

Article

Modified Gravity Description of Neutron Star in the $f(R)$ Framework

Samprity Das ^{1,2,†}, Irina Radinschi ^{3,†} and Surajit Chattopadhyay ^{2,*,†} 

¹ Department of Mathematics, Shibpur Dinobundhoo Institution (College), Shibpur, Howrah 711102, India

² Department of Mathematics, Amity University, Kolkata, New Town, Rajarhat, Kolkata 700135, India

³ Department of Physics, Gheorghe Asachi Technical University, 700050 Iasi, Romania

* Correspondence: surajitchatto@outlook.com or schattopadhyay1@kol.amity.edu

† These authors contributed equally to this work.

Abstract: The present paper reports a study on neutron stars in the $f(R)$ gravity framework for the Hu–Sawicki model, Starobinsky model, Tsujikawa model, and Exponential Gravity model. First, we have used the TOV equation for the $f(R)$ gravity framework, where we obtained two higher order differential equations for λ and ψ , with both functions depending on the radial coordinate. Furthermore, we have considered the BD theory, which is an equivalent theory of $f(R)$ gravity, and introduced a new scalar field ϕ_2 with the scalar potential $V(\phi_2)$. We have observed an increase in the scalar potential with respect to R in each case. Furthermore, our proposed models, namely quadratic form, exponential form, and linear form and the other viable models show a similar type of evolution for the scalar potential $V(\phi_2)$.

Keywords: neutron stars; $f(R)$ gravity; Hu–Sawicki model; Starobinsky model; Tsujikawa model; Exponential Gravity model

MSC: 85A40; 83F05



Citation: Das, S.; Radinschi, I.; Chattopadhyay, S. Modified Gravity Description of Neutron Star in the $f(R)$ Framework. *Axioms* **2023**, *12*, 234. <https://doi.org/10.3390/axioms12030234>

Academic Editor: Angel Ricardo Plastino

Received: 15 January 2023

Revised: 16 February 2023

Accepted: 19 February 2023

Published: 23 February 2023



Copyright: © 2023 by the authors. Licensee MDPI, Basel, Switzerland. This article is an open access article distributed under the terms and conditions of the Creative Commons Attribution (CC BY) license (<https://creativecommons.org/licenses/by/4.0/>).

1. Introduction

Accelerated universe expansion is the most mysterious and controversial research item in cosmology. The observation of a diminished optic wave represented the first evidence of the universe's accelerated expansion received from a Z-1 type 1A-supernova [1–3]. Some other verified data of accelerated expansion are Large-Scale Structure (LSS), Cosmic Microwave Background Radiation (CMBR), Galaxy Redshift, etc. [4–6]. All these data lead us to the existence of exotic matter having negative pressure and a non-clustered form in Large-Scale Structure named Dark Energy (DE) [7–10]. The equation of the state parameter for DE is $\omega = \frac{p}{\rho}$, which lies between (-1) and $(-1/3)$ and is named quintessence DE. For $\omega < -1$, one obtains the case of phantom DE. Though the exact nature of DE is still a different mystery, some models have been proposed to study the dynamic nature of DE. These are Chaplygin Gas model (CG) [11], Generalised Chaplygin Gas model (GCG) [12], Holographic Dark Energy Model (HDE) [13], Polytrropic Gas Model [14,15], K-essence model [16], etc. Now, Einstein's General Relativity (GR) cannot clarify the present state of the universe, which is greatly influenced by the existence of DE, dark matter (DM), and singularity. Astrophysicists must develop models for Modified GR [17–20], each with unique features to explain the present scenario and modified universe dynamics, but the matter part remains the same. Modified GR with high-density and large scalar curvature accurately defines the strong gravitational background. Modified GR, such as the $f(R)$ theory of gravity, contains a higher order differential function of the Ricci scalar R , which is a contraction of the Ricci tensor/the Riemann tensor. Furthermore, the Lagrangian in $f(R)$ contains a non-linear function of R [21]. Another important form of the Modified GR is $f(T)$ gravity, which can be derived by replacing the Ricci scalar R with the torsion

scalar T in $f(R)$ and obtain a comparatively less ordered differential function. This is the Teleparallel Equivalent of General Relativity (TEGR) [22]. The Modified GR helps to develop the idea of energy density in the form of a modified function of underlying gravity. Now, DE can be widely described using the Polytrropic Gas model [14,15]. The Polytrropic gas is obtained when the volume density relation remains constant for the gas in the case of expansion or contraction. The Polytrropic Gas model greatly impacts the study of the holographic DE models, the Chaplygin gas models, the scalar field models of GR, and the modified theory of gravity [23–26]. This paper uses the polytrropic gas model to explain the EOS degenerated Neutron Star (NS). Among all other astronomical objects, NS has a major impact on the cosmological study. Although it has a smaller surface area and radius, its massive baryonic density and immense gravitational force capture a huge amount of DM [27]. DM causes natural space to interact and eventually loses some energy. NS is an ideal cosmological laboratory for studying DM. There are different realistic models in the background of $f(R)$ gravity to investigate NS, such as (a) simple exponential model: $f(R) = R + \beta R(e^{-R/R_0} - 1)$ [where R_0 is constant] [28,29], (b) quadratic gravity model with logarithmic correlation with curvature: $f(R) = R + \alpha R^2(1 + \beta \log(R/\mu^2))$ [with $|\alpha| < 1$ and the dimensionless parameter $|\beta| < 1$], and (c) cubic correlation model: $f(R) = R + \alpha R^2(1 + \gamma R^2)$. A good choice of a viable model EOS is crucial for the existence of a stable star configuration. The stable star configuration exists with a high-density core (stability means $dm/d\rho_c > 0$ [30]). The minimum radius of such stars is close to 9 km for the maximal mass $\sim 1.9 M_\odot$ (SLy Equation [31]) or to the radius, 8.5 km for mass $\sim 1.7 M_\odot$ (FPS Equation [31]) [30]. The DM annihilation process occurs inside NS and sometimes, due to excess DM, NS crosses the Chandrasekhar limit [which is mass $\sim 1.44 M_\odot$ [32] for non-rotating compact object]. With higher temperatures, their outward radiation pressure cannot resist the interior gravitational pull and collapse under their weight and thus form a Black Hole (BH).

In Section 2, we have used the Tolmann–Oppenheimer–Volkoff (TOV) Equation, which is used to find equilibrium in a spherically symmetric body for isotropic material. TOV has established the upper limit of the gravitational mass of an NS using the EOS of degenerate cold Fermi gas [33]. Other than adopting any viable model in Section 2, we have considered the Ricci scalar R being expressed similar to some arbitrary functions of the radius. In this section, we have considered the equation of the state of the polytrropic gas model. We observed the evolution of $f(R)$ with the radius in a spherically symmetric body. In Section 3, we have used the Brans–Dicke theory, which is an equivalent form of $f(R)$ gravity with the scalar potential of gravitational origin [34,35]. The BD theory replaces the gravitational constant and establishes a new scalar field ϕ_2 in GR, which determines the distribution of mass–energy in the universe [36]. Here, the scalar ϕ_2 influences the universal matter that possesses nonminimal coupling [37,38] [coupling constant $Q = -1/\sqrt{6}$ [39]]. Study of the scalar potential $V(\phi_2)$ plays an important role in the NS and stability of a star. For the Starobinsky model, the potential can be defined as $V_E(\phi_2) = (3/4)m^2 M_{pl}^2 (1 - e^{-\sqrt{6}/(3M_{pl})\phi_2})^2$, where $V_E(\phi_2)$ is the potential for Einstein frame and $\phi_2 = (\sqrt{6}M_{pl}/2) \log(1 + R/3M^2)$ and M_{pl} reduced the Planck mass [39]. We also have adopted the arbitrary form of R and tried to observe the growth of the scalar potential with the change of radius. In Section 4, we study the important viable models of $f(R)$ gravity influenced by the work of K. Bamba [40]. These models preserve the stability conditions and the peculiar characteristics of the modified GR. As an exception, in this Section, we evaluated the evolution of the scalar potential in these special models for R (Ricci scalar).

2. The Tolman–Oppenheimer–Volkoff Equation for $f(R)$ Gravity

The Tolman–Oppenheimer–Volkoff equation is designed for a spherically symmetric body in the isotropic material that is in a gravitational equilibrium. We start this Section

with the $f(R)$ gravity framework for a spherically symmetric compact object and the corresponding TOV equation. The $f(R)$ actions is provided by

$$\mathcal{A} = \frac{c^4}{16\pi G} \int d^4x \sqrt{-g}(f(R) + \mathcal{L}_{matter}), \tag{1}$$

where g is the determinant of the metric $g_{\mu\nu}$ and \mathcal{L}_{matter} is the standard perfect fluid matter term in Lagrangian. The variation of Equation (1) with respect to $g_{\mu\nu}$ provides the field Equation [41–43]

$$\frac{df(R)}{dR} R_{\mu\nu} - \frac{1}{2}f(R)g_{\mu\nu} - \frac{(\nabla_\mu \nabla_\nu - g_{\mu\nu} \square)df(R)}{dR} = \frac{8\pi G}{c^4} T_{\mu\nu}, \tag{2}$$

where

$$T_{\mu\nu} = \frac{-2}{\sqrt{-g}} \frac{\delta(\sqrt{-g}\mathcal{L}_m)}{\delta g^{\mu\nu}}, \tag{3}$$

is the energy momentum tensor of the matter. The metric for systems with spherical symmetry has the usual form

$$ds^2 = e^{2\psi} c^2 dt^2 - e^{2\lambda} dr^2 - r^2 (d\theta^2 + \sin^2\theta d\phi^2), \tag{4}$$

where ψ and λ are functions of radial coordinate r [44]. The energy–momentum tensor of a matter that is described as a perfect fluid within a star is

$$T_{\mu\nu} = \text{diag}(e^{2\psi} \rho c^2, e^{2\lambda} p, r^2 p, r^2 p \sin^2\theta). \tag{5}$$

Here, p and ρ are the matter pressure and density, respectively, [45]. The Euler Conservation Energy is

$$\frac{dp}{dr} = \frac{-(\rho + p)d\psi}{dr}. \tag{6}$$

From the metric provided by Equation (4) and the field Equation (2), one obtains ψ and λ derived with respect to r of the form [46]

$$\frac{d\lambda}{dr} = \frac{e^{2\lambda}(r^2(16\pi\rho + f(R)) - f'(R)(r^2R + 2)) + 2R_r^2 f'''(R)r^2 + 2rf''(R)(rR_{r,r} + 2R_r) + 2f'(R)}{2r(2f'(R) + rR_r f''(R))}, \tag{7}$$

and

$$\frac{d\psi}{dr} = \frac{e^{2\lambda}(r^2(16\pi\rho - f(R)) + f'(R)(r^2R + 2)) - 2(2rf''(R)R_r + f'(R))}{2r(2f'(R) + rR_r f''(R))}. \tag{8}$$

Here, $f'(R)$, $f''(R)$, and $f'''(R)$ denote the first-order, second-order, and third-order derivatives of $f(R)$, respectively, concerning Ricci scalar $R(r)$. The above equations are modified TOV equations, and, as the Ricci scalar, R is a dynamical variable in $f(R)$ gravity, so we need further equations to solve Equations (6)–(8). Using the trace of Equation (2) and inserting it in metric Equation (4) we derive an equation of the form

$$\frac{d^2R}{dr^2} = R_r \left(\lambda_r + \frac{1}{r} \right) + \frac{f'(R)}{f''(R)} \left(\frac{1}{r} \left(3\psi_r - \lambda_r + \frac{2}{r} \right) - e^{2\lambda} \left(\frac{R}{2} + \frac{2}{r^2} \right) \right) - \frac{R_r^2 f'''(R)}{f''(R)}. \tag{9}$$

We use the polytropic gas model to explain the EOS of degenerated Neutron Star [47]

$$p_\Lambda = K\rho_\Lambda^{1+\frac{1}{n_1}}, \tag{10}$$

where η_1 is the polytropic index and K is a positive constant. To solve the equations, we use λ and ψ in power law form as follows

$$\psi = \psi_0 r^{\eta_2}, \tag{11}$$

$$\lambda = \lambda_0 r^{\eta_3}. \tag{12}$$

At this point, it is worth mentioning that the power law form is a well-discussed assumption in various astrophysical modeling. For example, in [48,49], where power law forms have been adopted for a modified gravity and GW energy spectrum, respectively. Motivated by these works, we adopted power law forms of functions of radial coordinates in our modeling. A similar approach has been adopted in our subsequent choice of $f(R)$, where R would be adopted as a polynomial with r raised to different powers. In this context, let us mention that the power law form of $f(R)$ gravity with R raised to higher powers has been demonstrated in [48], and, in our work, we would express R as a function of r and the polynomial would be on r . Furthermore, a choice of R in the exponential form [50] would also be experimented with for its viability in the given framework of neutron star under the purview of the modified theory of gravity.

From Equations (10)–(12), we obtain the derivatives of p_Λ , ψ , and λ with respect to r

$$\frac{dp_\Lambda}{dr} = K \left(1 + \frac{1}{\eta_1} \right) \rho_\Lambda^{\frac{1}{\eta_1}} \frac{d\rho_\Lambda}{dr}, \tag{13}$$

$$\frac{d\psi}{dr} = \psi_0 \eta_2 r^{\eta_2-1}, \tag{14}$$

$$\frac{d\lambda}{dr} = \lambda_0 \eta_3 r^{\eta_3-1}. \tag{15}$$

From Equations (6), (13), and (14), the value of ρ_Λ can be found as

$$\rho_\Lambda = \left(\frac{-1 + e^{\frac{-r^{\eta_2} \eta_1 \Psi_0 + K C_1 + K \eta_1 C_1}{\eta_1 + \eta_1^2}}}{K} \right)^{\eta_1}. \tag{16}$$

To study the pattern of $f(R)$, we use different expressions of R as a function of r (radius).

2.1. R as a Quadratic Function of Radius

Now, we consider $R(r)$ being in the quadratic form, to find the other values of $f(R)$

$$R = a_0 + a_1 r + a_2 r^2. \tag{17}$$

Here, a_0 , a_1 , and a_2 are arbitrary constants. Thus, $f(R)$ is converted as $f(R(r))$. Equations (7)–(9) can be rewritten as

$$\frac{d\lambda}{dr} = \frac{e^{2\lambda} (r^2(16\pi\rho + f(r)) - f'(r)(r^2(a_0 + a_1 r + a_2 r^2) + 2)) + 2(a_1 + 2a_2 r)^2 f'''(r)r^2 + 2r f''(r)(2ra_2 + 2(a_1 + 2a_2 r)) + 2f'(r)}{2r(2f'(r) + r(a_1 + 2a_2 r)f''(r))}, \tag{18}$$

$$\frac{d\psi}{dr} = \frac{e^{2\lambda} (r^2(16\pi\rho - f(r)) + f'(r)(r^2(a_0 + a_1 r + a_2 r^2) + 2)) - 2[2r f''(r)(a_1 + 2a_2 r) + f'(r)]}{2r(2f'(r) + (a_1 + 2a_2 r)r f''(r))}, \tag{19}$$

$$\frac{d^2 R}{dr^2} = (a_1 + 2a_2 r) \left(\lambda_r + \frac{1}{r} \right) + \frac{f'(r)}{f''(r)} \left(\frac{1}{r} \left(3\psi_r - \lambda_r + \frac{2}{r} \right) - e^{2\lambda} \left(\frac{(a_0 + a_1 r + a_2 r^2)}{2} + \frac{2}{r^2} \right) \right) - \frac{(a_1 + 2a_2 r)^2 f'''(r)}{f''(r)}. \tag{20}$$

Now, we find the solution set of $f(R(r))$ by solving Equations (18), (12), (15), and (16) and the corresponding graphs for different values of $\lambda_0, \Psi_0, \eta_1, \eta_2, \eta_3, a_0, a_1, a_2, K,$ and C_1 are displayed in Figure 1.

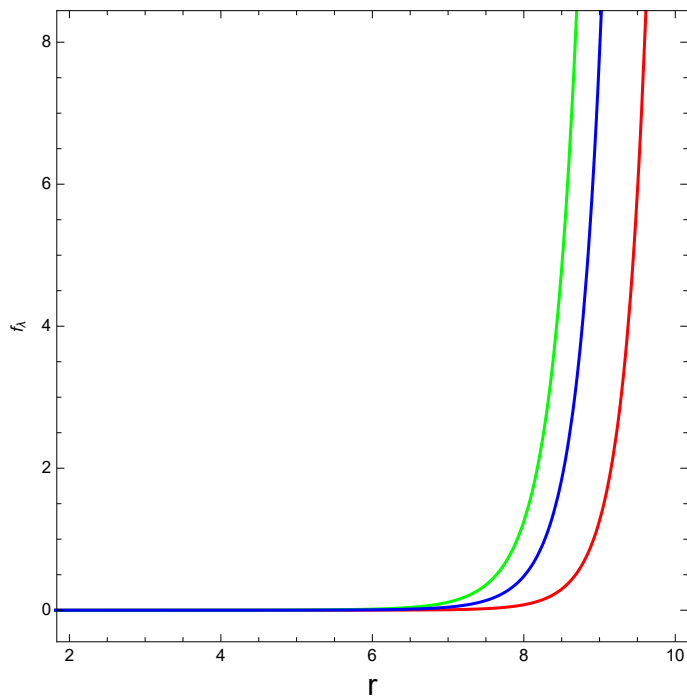


Figure 1. Solution of $f(R(r))$ for R adopted as a quadratic function of radius. The evolution of Equation (7) under $f(R(r))$ gravity is presented. We have fixed the values of $\eta_2, \eta_3, a_0, a_1, a_2, K,$ and C_1 . The red, green, and blue lines correspond to small perturbations of $\lambda_0, \Psi_0,$ and $\eta_1,$ respectively.

Solving Equations (19), (11), (14), and (16), we found a solution set of $f(R(r))$ and the corresponding plot for different values of $\lambda_0, \Psi_0, \eta_1, \eta_2, \eta_3, a_0, a_1, a_2, K,$ and C_1 in Figure 2.

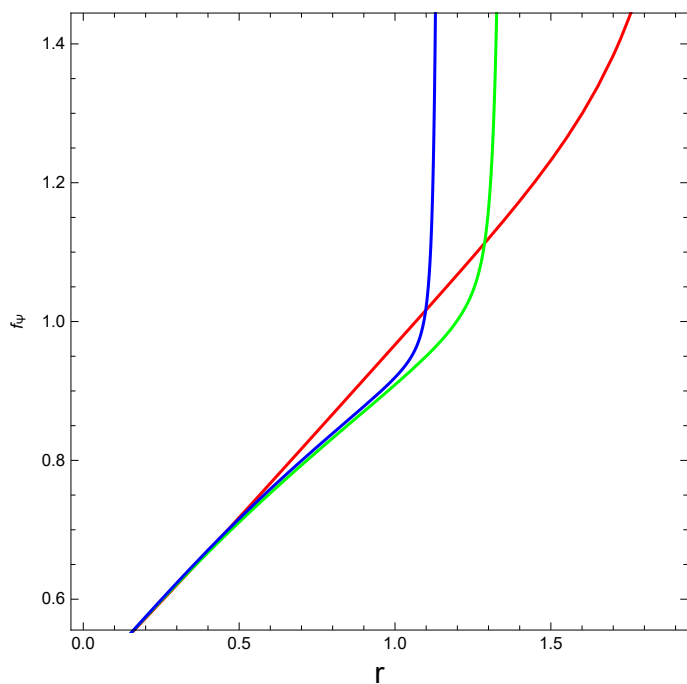


Figure 2. Solution of $f(R(r))$ for R adopted as a quadratic function of radius. The evolution of Equation (8) under $f(R(r))$ gravity is shown. We have fixed the values of $a_0, a_1, a_2, K,$ and C_1 . The red, green, and blue lines correspond to small perturbations of $\lambda_0, \Psi_0, \eta_1, \eta_2,$ and $\eta_3,$ respectively.

2.2. R as an Exponential Function of Radius

Now, we express $R(r)$ in an exponential form to find further derivatives of $f(R)$ as

$$R = \alpha e^r + \beta e^{-r}, \tag{21}$$

where α, β are arbitrary constants. In this case, Equations (7)–(9) can be rewritten as

$$\frac{d\lambda}{dr} = \frac{e^{2\lambda} (r^2(16\pi\rho + f(r)) - f'(r)(r^2(\alpha e^r + \beta e^{-r}) + 2)) + 2(\alpha e^r - \beta e^{-r})^2 f'''(r)r^2 + 2rf''(r)(r(\alpha e^r + \beta e^{-r}) + 2(\alpha e^r - \beta e^{-r})) + 2f'(r)}{2r(2f'(r) + r(\alpha e^r - \beta e^{-r})f''(r))}, \tag{22}$$

$$\frac{d\psi}{dr} = \frac{e^{2\lambda} [r^2(16\pi\rho - f(r)) + f'(r)(r^2(\alpha e^r + \beta e^{-r}) + 2)] - 2[2rf''(r)(\alpha e^r - \beta e^{-r}) + f'(r)]}{2r[2f'(r) + (\alpha e^r - \beta e^{-r})rf''(r)]}, \tag{23}$$

$$\frac{d^2R}{dr^2} = (\alpha e^r - \beta e^{-r}) \left(\lambda_r + \frac{1}{r} \right) + \frac{f'(r)}{f''(r)} \left[\frac{1}{r} \left(3\psi_r - \lambda_r + \frac{2}{r} \right) - e^{2\lambda} \left(\frac{(\alpha e^r + \beta e^{-r})}{2} + \frac{2}{r^2} \right) \right] - \frac{(\alpha e^r - \beta e^{-r})^2 f'''(r)}{f''(r)}. \tag{24}$$

Solving Equations (22), (12), (15), and (16), we found a solution set of $f(R(r))$ and the corresponding graph for different values of $\lambda_0, \Psi_0, \eta_1, \eta_2, \eta_3, a_0, a_1, a_2, K,$ and C_1 in Figure 3.

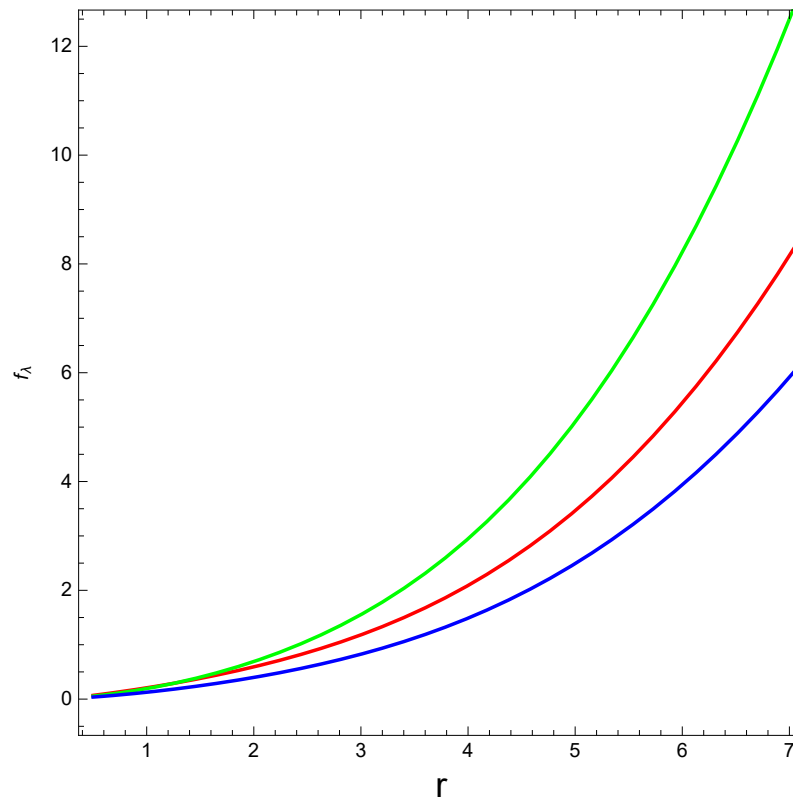


Figure 3. Solution of $f(R(r))$ for R adopted as an exponential function of radius. The evolution of Equation (7) under $f(R(r))$ gravity is provided. We have fixed the values of $\eta_2, \eta_3, a_0, a_1, a_2, K,$ and C_1 . The red, green, and blue lines correspond to small perturbations of $\lambda_0, \Psi_0,$ and $\eta_1,$ respectively.

Solving Equations (23), (11), (14), and (16), we obtained a solution set of $f(R(r))$ and the corresponding graph for different values of $\lambda_0, \Psi_0, \eta_1, \eta_2, \eta_3, a_0, a_1, a_2, K,$ and C_1 in Figure 4.

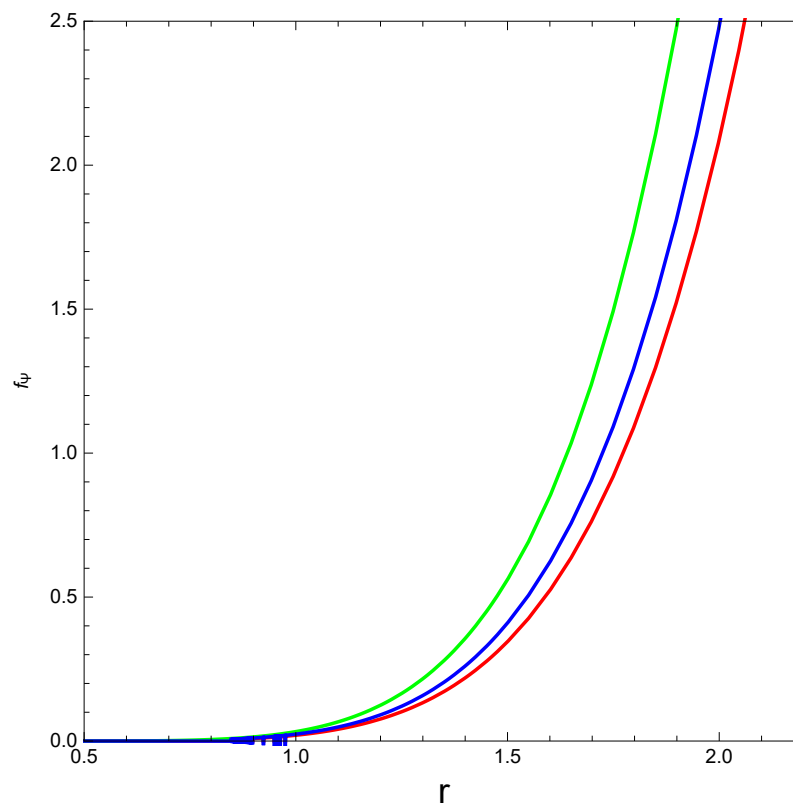


Figure 4. Solution of $f(R(r))$ for R is expressed as an exponential function of radius. The evolution of Equation (8) under $f(R(r))$ gravity is provided. We have fixed the values of $a_0, a_1, a_2, K,$ and C_1 . The red, green, and blue lines correspond to small perturbations of $\lambda_0, \Psi_0, \eta_1, \eta_2,$ and $\eta_3,$ respectively.

2.3. R as a Linear Function of Radius

Now, we consider $R(r)$ being of the linear form, to find the other values of $f(R)$.

$$R = b_0 + b_1 r. \tag{25}$$

Here b_0, b_1 are arbitrary constants. Thus, $f(R)$ converted as $f(R(r))$ and further Equations (7)–(9) can be rewritten as

$$\frac{d\lambda}{dr} = \frac{e^{2\lambda} (r^2(16\pi\rho + f(r)) - f'(r)(r^2(b_0 + b_1 r) + 2)) + 2(b_1)^2 f'''(r)r^2 + 2r f''(r)(2(b_1)) + 2f'(r)}{2r(2f'(r) + r(b_1)f''(r))}, \tag{26}$$

$$\frac{d\psi}{dr} = \frac{e^{2\lambda} (r^2(16\pi\rho - f(r)) + f'(r)(r^2(b_0 + b_1 r) + 2)) - 2(2r f''(r)(b_1) + f'(r))}{2r(2f'(r) + (b_1)r f''(r))}, \tag{27}$$

$$\frac{d^2 R}{dr^2} = (b_1) \left(\lambda_r + \frac{1}{r} \right) + \frac{f'(r)}{f''(r)} \left(\frac{1}{r} \left(3\psi_r - \lambda_r + \frac{2}{r} \right) - e^{2\lambda} \left(\frac{(b_0 + b_1 r)}{2} + \frac{2}{r^2} \right) \right) - \frac{(b_1)^2 f'''(r)}{f''(r)}. \tag{28}$$

Solving Equations (26), (12), (15), and (16), we obtained a solution set of $f(R(r))$ and the corresponding graph for different values of $\lambda_0, \Psi_0, \eta_1, \eta_2, \eta_3, a_0, a_1, a_2, K,$ and C_1 in Figure 5.

Solving Equations (27), (11), (14), and (16), we obtain a solution set of $f(R(r))$ and the corresponding graph for different values of $\lambda_0, \Psi_0, \eta_1, \eta_2, \eta_3, a_0, a_1, a_2, K,$ and C_1 in Figure 6.

In Figures 1, 3 and 5, we observe that the $f(R)$ gravity for Equation (7) presents an ascending pattern with respect to r . The considered functions become significantly different shapes of figures. In each case, there is an ascending pattern observed. Thus, $f(R)$ gravity will show an increasing pattern with r . Figures 1 and 5 show that, after a certain value of r , $f(R)$ has a sharply increasing pattern.

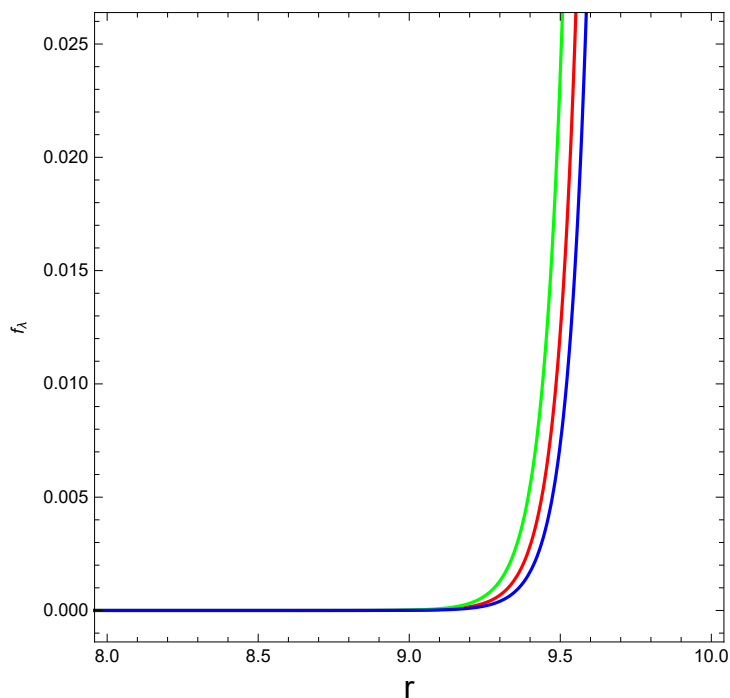


Figure 5. Solution of $f(R(r))$ for R adopted as a linear function of radius. The evolution of Equation (7) under $f(R(r))$ gravity is provided. We have fixed the values of $\eta_2, \eta_3, a_0, a_1, a_2, K,$ and C_1 . The red, green, and blue lines correspond to small perturbations of $\lambda_0, \Psi_0,$ and $\eta_1,$ respectively.

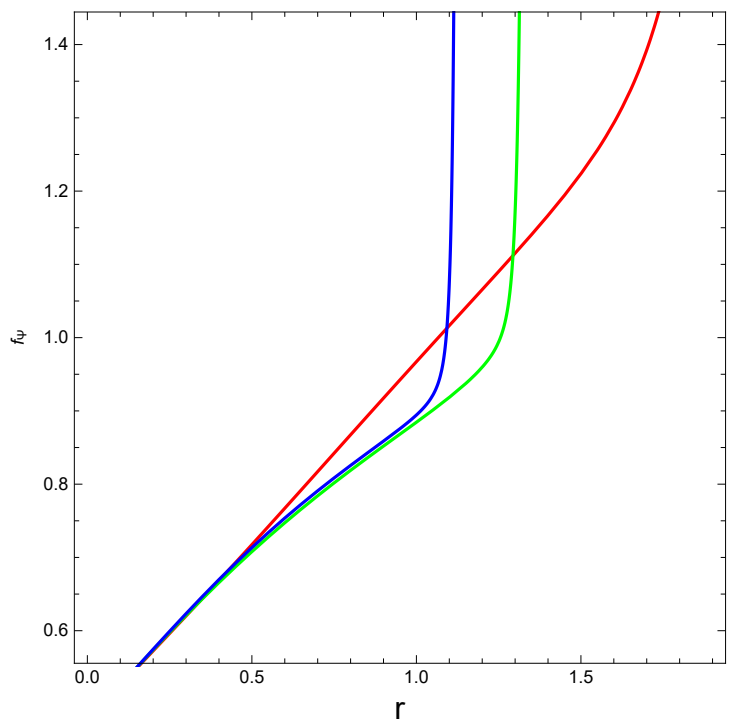


Figure 6. Solution of $f(R(r))$ for R adopted as a linear function of radius. The evolution of Equation (8) under $f(R(r))$ gravity is provided. We have fixed the values of $a_0, a_1, a_2, K,$ and C_1 . The red, green, and blue lines correspond to small perturbations of $\lambda_0, \Psi_0, \eta_1, \eta_2,$ and $\eta_3,$ respectively.

In Figures 2, 4 and 6 note that the $f(R)$ gravity for Equation (8) has an ascending pattern with respect to r . We obtain different ascending patterns for R being quadratic, exponential, and linear functions of radius. Though, for the quadratic function and linear function, the pattern of the graph is similar. This shows that $f(R)$ gravity keeps increasing for larger values of the radius.

3. The Brans–Dicke Theory for $f(R)$ Gravity

Let us start with the action of scalar–tensor theories accommodating BD theories with a scalar potential $V(\phi_2)$ [51]

$$S = \int d^4x \sqrt{-g} \left(\frac{M_{pl}^2}{2} F(\phi_2) R + (1 - 6Q^2) F(Q) X - V(\phi_2) \right) + \int d^4x \mathcal{L}_m(g_{\mu\nu}, \psi_m), \tag{29}$$

where g is the determinant of the metric $g_{\mu\nu}$, $F(\phi_2)$ is the function of the scalar field ϕ_2 , R is the Ricci scalar, Q is the constant characterizes the coupling between ϕ_2 and the gravity, and $X = -g^{\mu\nu} \partial_\mu \phi \partial_\nu \phi / 2$ and \mathcal{L}_m are the action of matter field ψ_m [52]. The potential that corresponds to the nonminimal coupling according to the BD theories is

$$F(\phi_2) = e^{-2Q\phi_2/M_{pl}}. \tag{30}$$

The $f(R)$ gravity provided by the action belongs to the gravitational scalar action of Equation (29) [53]

$$S_{f(R)} = \int d^4x \sqrt{-g} \frac{M_{pl}^2}{2} F(R). \tag{31}$$

Here, $f(R)$ contains nonlinear function of R and ϕ_2 is the scalar degree of freedom. The field potential $V(\phi_2)$ does not vanish, so the field ϕ_2 has an effect on the mass. We have $Q = -1/\sqrt{6}$

$$V(\phi_2) = \frac{M_{pl}^2}{2} (FR - f), \tag{32}$$

where

$$F = \frac{\partial f}{\partial R}. \tag{33}$$

For different expressions of the Ricci scalar R as a function of radius, we obtain different values of F and scalar potential $V(\phi_2)$.

3.1. The Scalar Potential for R as a Quadratic Function of Radius

Now, we are adopting $R(r)$ of the quadratic form to find the other values of F and $V(\phi_2)$. For the form of R in Equation (17) F can be transformed as

$$F = \frac{\partial f}{\partial r} \left(\frac{1}{a_1 + 2a_2 r} \right) \tag{34}$$

and $V(\phi_2)$ can be transformed to

$$V(\phi_2) = \frac{1}{2} \left(\frac{\partial f}{\partial r} \left(\frac{a_0 + a_1 r + a_2 r^2}{a_1 + 2a_2 r} \right) - f \right). \tag{35}$$

From the solutions set of $f(r)$ and Equation (33), we deduce the solutions set of $F(R)$. Comparing Equation (7) with Equation (36), Equation (38), and Equation (46), we obtain one set of graphical representations of $F(R)$ for different values of $\lambda_0, \Psi_0, \eta_1, \eta_2, \eta_3, a_0, a_1, a_2, K$, and C_1 in Figure 7.

Again, comparing Equation (8) with Equation (36), Equation (38), and Equation (46), we obtain one set of graphical representations of $F(R)$ for different values of $\lambda_0, \Psi_0, \eta_1, \eta_2, \eta_3, a_0, a_1, a_2, K$, and C_1 in Figure 8.

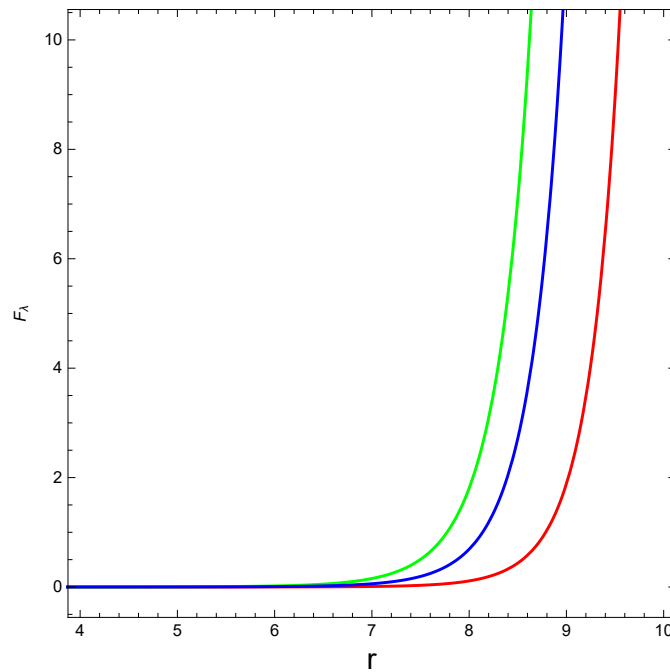


Figure 7. Solution of $F(R(r))$ for R adopted as quadratic function of radius. The evolution of the partial derivative of $f(R)$ is obtained by Equations (7) and (33). We have fixed the values of $\eta_2, \eta_3, a_0, a_1, a_2, K,$ and C_1 . The red, green, and blue lines correspond to small perturbations of $\lambda_0, \Psi_0, \eta_1,$ respectively.

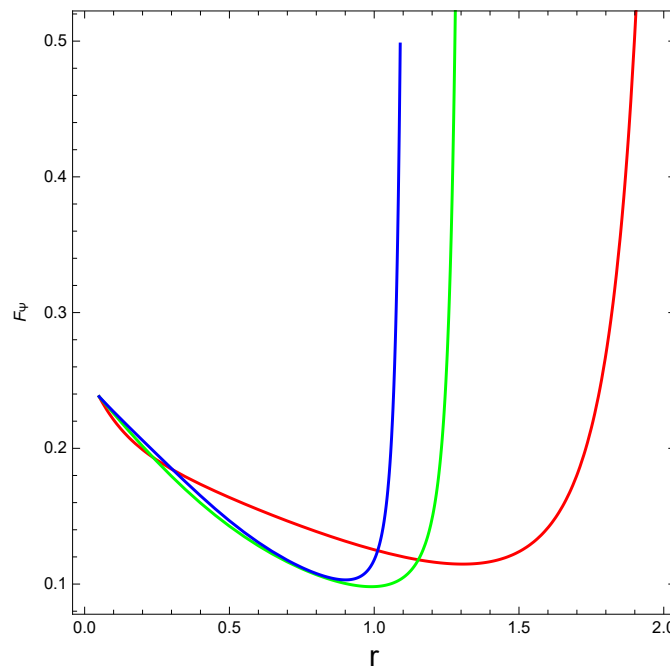


Figure 8. Solution of $F(R(r))$ for R adopted as a quadratic function of radius. The evolution of the partial derivative of $f(R)$ is obtained by Equations (8) and (33). We have fixed the values of $a_0, a_1, a_2, K,$ and C_1 . The red, green, and blue lines correspond to small perturbations of $\lambda_0, \Psi_0, \eta_1, \eta_2,$ and $\eta_3,$ respectively.

The graphical representation of the scalar potential is shown by comparing Equation (7) and Equation (32). For three different expressions of the Ricci scalar (R), the solutions set of f provides different forms. Comparing Equation (7) with Equation (35), Equation (37), and Equation (39), we obtain the plot for different values of $\lambda_0, \Psi_0, \eta_1, \eta_2, \eta_3, a_0, a_1, a_2, K,$ and C_1 in Figure 9.

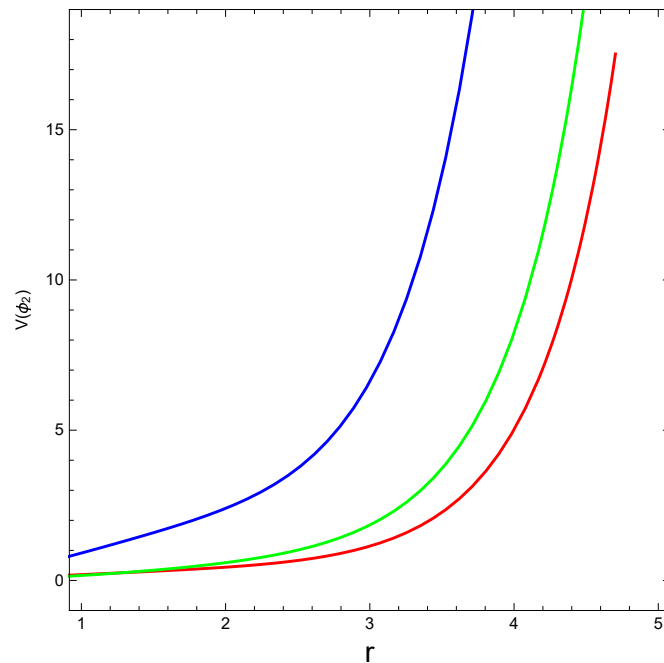


Figure 9. Solution of the scalar potential for R adopted as a quadratic function of radius. The evolution of the scalar potential $V(\phi_2)$ is obtained by Equations (7) and (32). We have fixed the values of $\eta_2, \eta_3, a_0, a_1, a_2, K,$ and C_1 . The red, green, and blue lines correspond to small perturbations of $\lambda_0, \Psi_0,$ and η_1 , respectively.

Now, comparing Equation (8) and Equation (32), the corresponding set of the scalar potentials has been represented graphically. Here, three different forms of the Ricci scalar have also been used to draw the conclusion. By comparing Equation (8) with Equation (35), Equation (37), and Equation (39) and using the solution sets of $f(R)$, we obtain the graphical representation for different values of $\lambda_0, \Psi_0, \eta_1, \eta_2, \eta_3, a_0, a_1, a_2, K,$ and C_1 in Figure 10.

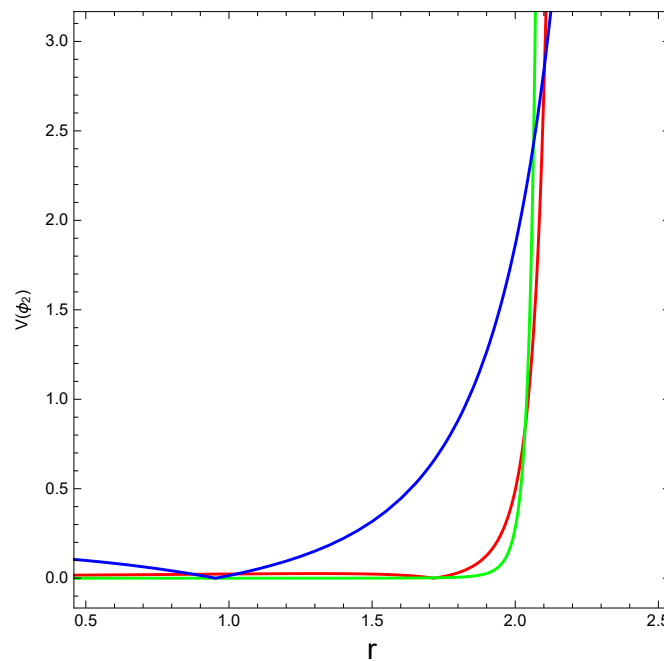


Figure 10. Solution of the scalar potential for R adopted as a quadratic function of radius. The evolution of the scalar potential $V(\phi_2)$ is presented by Equations (8) and (32). We have fixed the values of $a_0, a_1, a_2, K,$ and C_1 . The red, green, and blue lines correspond to small perturbations of $\lambda_0, \Psi_0, \eta_1, \eta_2,$ and η_3 , respectively.

3.2. The Scalar Potential for R as an Exponential Function of Radius

We consider $R(r)$ being of the exponential form, to find further derivations of $F(R)$ and $V(\phi_2)$. The Ricci scalar R provided in Equation (21) F can be transformed as

$$F = \frac{\partial f}{\partial r} \left(\frac{1}{\alpha e^r - \beta e^{-r}} \right) \tag{36}$$

and $V(\phi_2)$ can be transformed to

$$V(\phi_2) = \frac{1}{2} \left(\frac{\partial f}{\partial r} \frac{\alpha e^r + \beta e^{-r}}{\alpha e^r - \beta e^{-r}} - f \right). \tag{37}$$

From the solution set of $f(r)$ and Equation (33) we deduce the solution set of $F(R)$. By comparing Equation (7) with Equation (36), Equation (38), and Equation (46), we present the plot of $F(R)$ for different values of $\lambda_0, \Psi_0, \eta_1, \eta_2, \eta_3, a_0, a_1, a_2, K$, and C_1 in Figure 11.

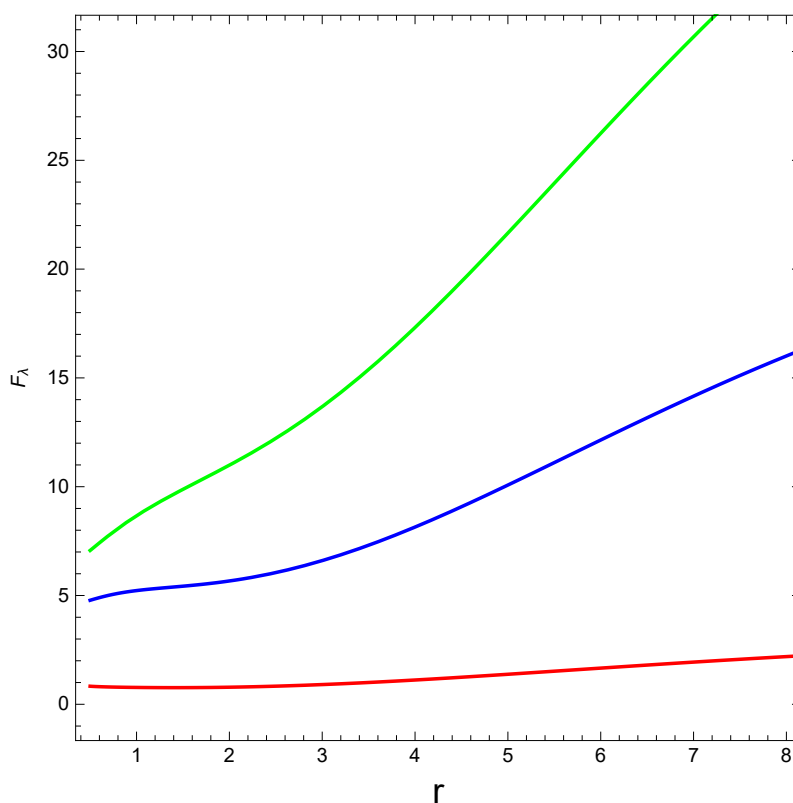


Figure 11. Solution of $F(R(r))$ for R adopted as an exponential function of radius. The evolution of partial derivative of $f(R)$ is presented by comparing Equation (7) and Equation (33). We have fixed the values of $\eta_2, \eta_3, a_0, a_1, a_2, K$, and C_1 . The red, green, and blue lines correspond to small perturbations of λ_0, Ψ_0 , and η_1 , respectively.

Once again, from the comparison of Equation (8) with Equation (36), Equation (38), and Equation (46), we plot the graph of $F(R)$ for different values of $\lambda_0, \Psi_0, \eta_1, \eta_2, \eta_3, a_0, a_1, a_2, K$, and C_1 in Figure 12.

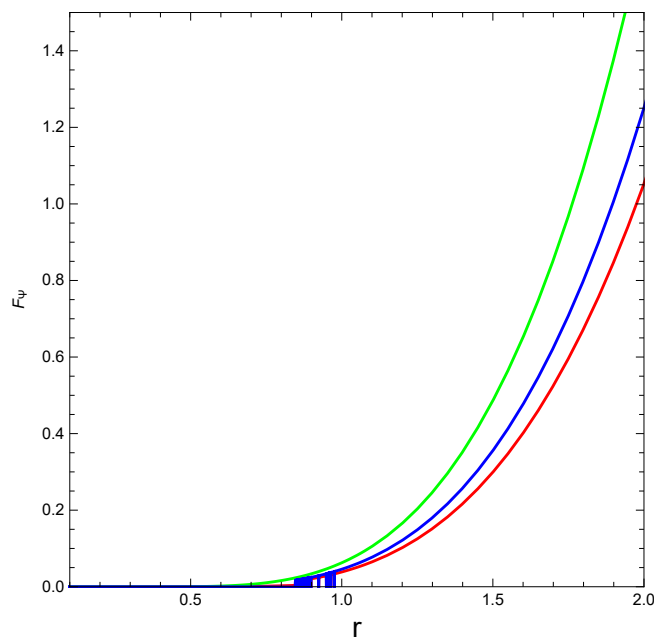


Figure 12. Solution of $F(R(r))$ for R adopted as an exponential function of radius. The evolution of partial derivative of $f(R)$ is obtained by comparing Equation (8) and Equation (33). We have fixed the values of $a_0, a_1, a_2, K,$ and C_1 . The red, green, and blue lines correspond to small perturbations of $\lambda_0, \Psi_0, \eta_1, \eta_2,$ and $\eta_3,$ respectively.

We show the graph of the scalar potential by comparing Equation (7) and Equation (32). For three different forms of the Ricci scalar (R), the solution set of f provides different forms. By comparing Equation (7) with Equation (35), Equation (37), and Equation (39), we obtain the graphical representation for different values of $\lambda_0, \Psi_0, \eta_1, \eta_2, \eta_3, a_0, a_1, a_2, K,$ and C_1 in Figure 13.

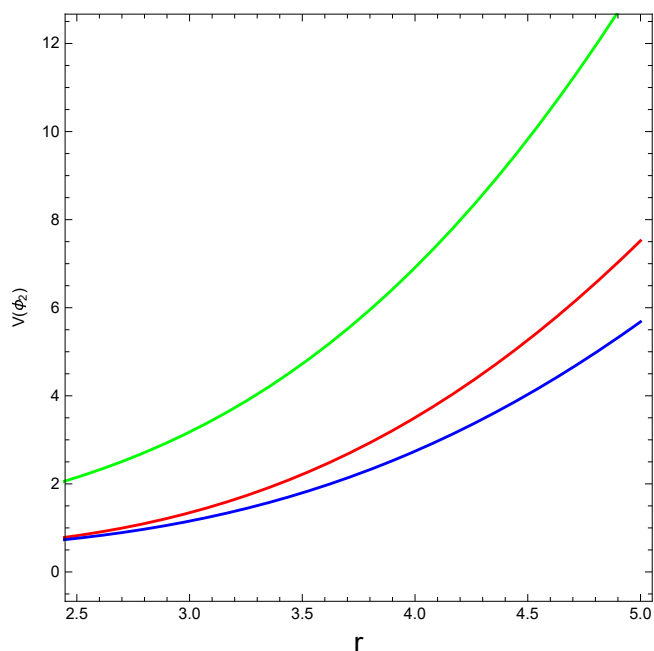


Figure 13. Solution of the scalar potential for R adopted as an exponential function of radius. The evolution of the scalar potential $V(\phi_2)$ is obtained by comparing Equation (7) and Equation (32). We have fixed the values of $\eta_2, \eta_3, a_0, a_1, a_2, K,$ and C_1 . The red, green, and blue lines correspond to small perturbations of $\lambda_0, \Psi_0,$ and $\eta_1,$ respectively.

From the comparison of Equation (8) and Equation (32) another set of the scalar potential has been represented graphically. Here, three different forms of the Ricci scalar have also been used to draw the conclusion. Comparing Equation (8) with Equation (35), Equation (37), and Equation (39) and with the solution set of $f(R)$, we obtain the graphical representation for different values of $\lambda_0, \Psi_0, \eta_1, \eta_2, \eta_3, a_0, a_1, a_2, K$, and C_1 in Figure 14.

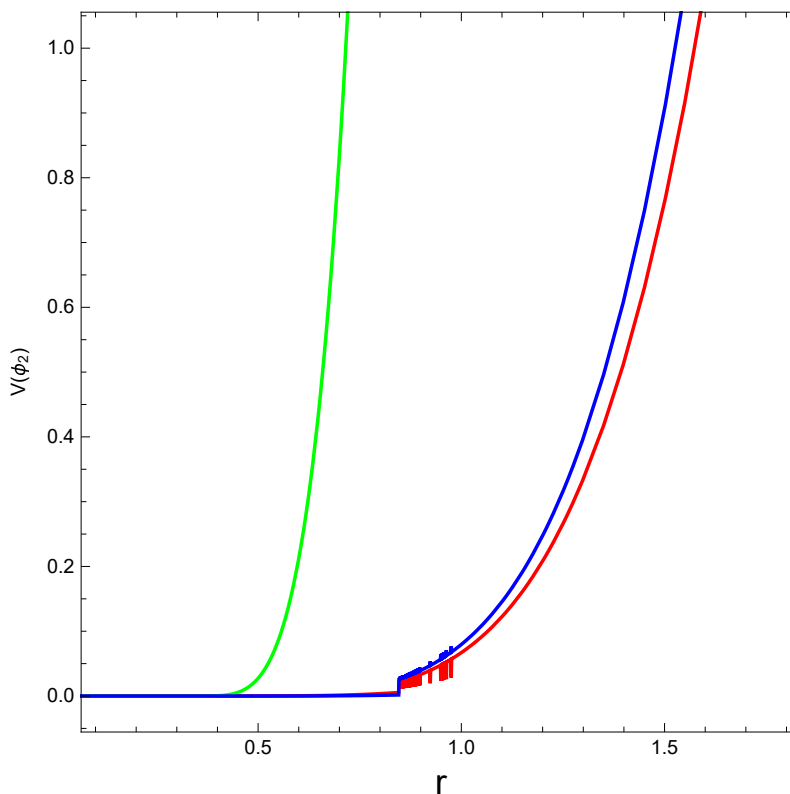


Figure 14. Solution of the scalar potential for R is adopted as an exponential function of radius. The evolution of scalar potential $V(\phi_2)$ comparing Equation (8) and Equation (32). We have fixed the values of a_0, a_1, a_2, K , and C_1 . The red, green, and blue lines correspond to small perturbations of $\lambda_0, \Psi_0, \eta_1, \eta_2$, and η_3 , respectively.

3.3. The Scalar Potential for R as a Linear Function of Radius

Considering $R(r)$ as the linear form, we found other values of $F(R)$ and $V(\phi_2)$. For the form of R from Equation (25) F can be transformed as

$$F = \frac{\partial f}{\partial r} \left(\frac{1}{b_1} \right) \tag{38}$$

and $V(\phi_2)$ can be transformed to

$$V(\phi_2) = \frac{1}{2} \left(\frac{\partial f}{\partial r} \left(\frac{b_0 + b_1 r}{b_1} \right) - f \right). \tag{39}$$

From the set of solutions of $f(r)$ and Equation (33), we deduce the set of solutions of $F(R)$. By comparing Equation (7) with Equation (36), Equation (38), and Equation (46), we obtain the graphical representation of $F(R)$ for different values of $\lambda_0, \Psi_0, \eta_1, \eta_2, \eta_3, a_0, a_1, a_2, K$, and C_1 in Figure 15.

From the comparison of Equation (8) with Equation (36), Equation (38), and Equation (46) we obtained one set of graphical representations of $F(R)$ for different values of $\lambda_0, \Psi_0, \eta_1, \eta_2, \eta_3, a_0, a_1, a_2, K$, and C_1 in Figure 16.

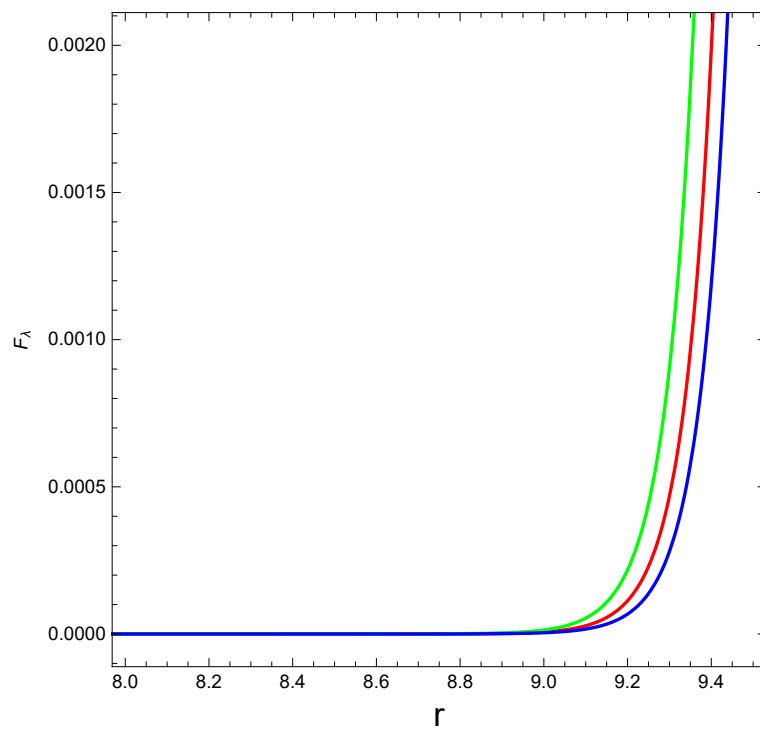


Figure 15. Solution of $F(R(r))$ for R adopted as a linear function of radius. The evolution of partial derivative of $f(R)$ is obtained by comparing Equation (7) and Equation (33). We have fixed the values of $\eta_2, \eta_3, a_0, a_1, a_2, K,$ and C_1 . The red, green, and blue lines correspond to small perturbations of $\lambda_0, \Psi_0,$ and $\eta_1,$ respectively.

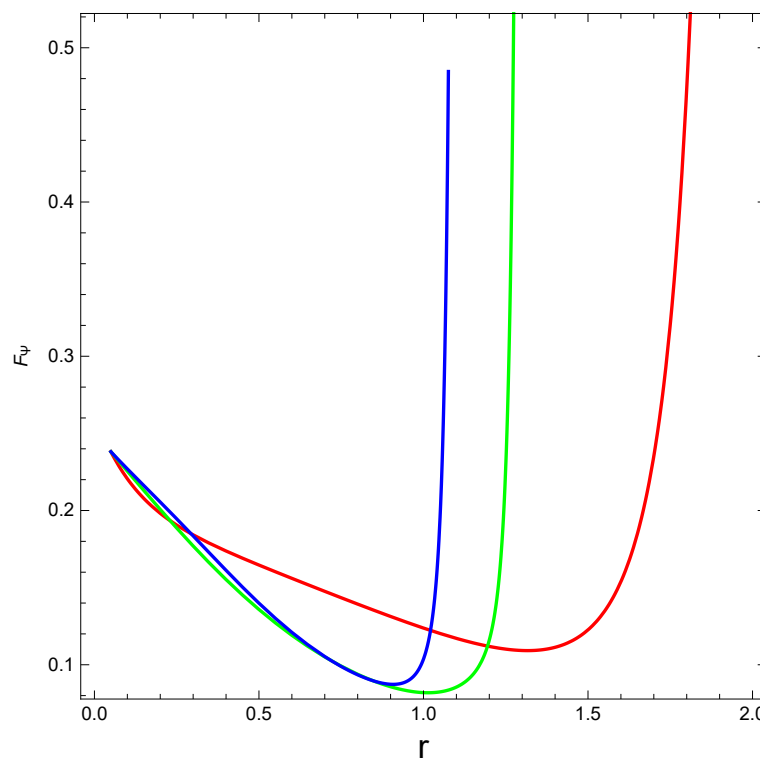


Figure 16. Solution of $F(R(r))$ for R adopted as a linear function of radius. The evolution of partial derivative of $f(R)$ is provided by comparing Equation (8) and Equation (33). We have fixed the values of $a_0, a_1, a_2, K,$ and C_1 . The red, green, and blue lines correspond to small perturbations of $\lambda_0, \Psi_0, \eta_1, \eta_2,$ and $\eta_3,$ respectively.

Now, the graphical representation of the scalar potential can be shown by comparing Equation (7) and Equation (32). For three different forms of the Ricci scalar (R), the solution set of f provides different forms. Comparing Equation (7) with Equation (35), Equation (37), and Equation (39), we obtain the following graphical representation for different values of λ_0 , Ψ_0 , η_1 , η_2 , η_3 , a_0 , a_1 , a_2 , K , and C_1 in Figure 17.

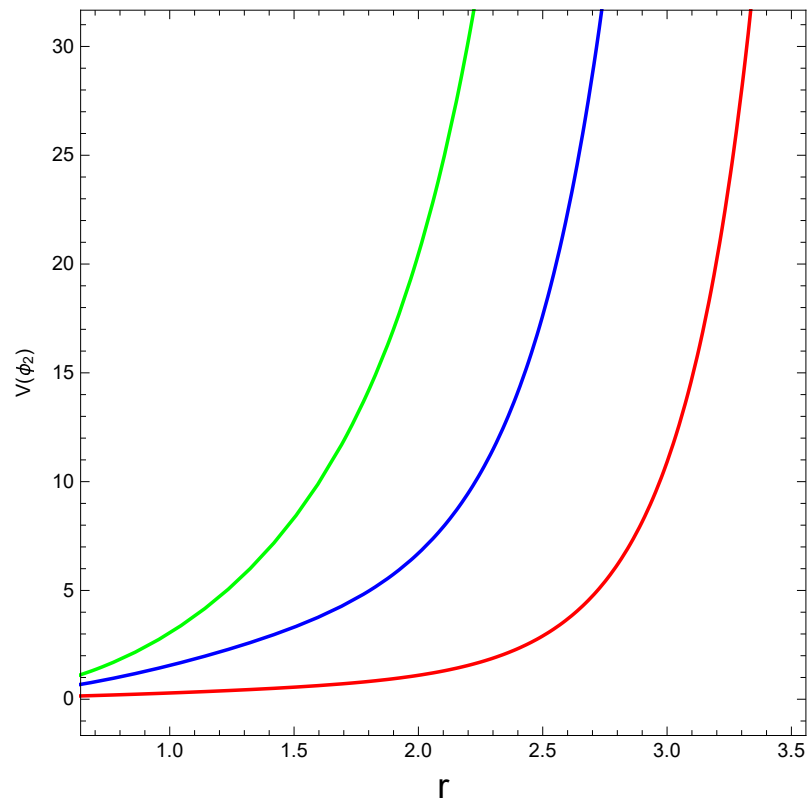


Figure 17. Solution of the scalar potential for R adopted as a linear function radius. The evolution of the scalar potential $V(\phi_2)$ is obtained by comparing Equation (7) and Equation (32). We have fixed the values of η_2 , η_3 , a_0 , a_1 , a_2 , K , and C_1 . The red, green, and blue lines correspond to small perturbations of λ_0 , Ψ_0 , and η_1 , respectively.

Comparing Equation (8) and Equation (32), another set of scalar potential has been represented graphically. Here, three different forms of the Ricci scalar have also been used to draw the conclusion. By comparing Equation (8) with Equation (35), Equation (37), and Equation (39) and with the solution set of $f(R)$, we obtain the following graphical representation for different values of λ_0 , Ψ_0 , η_1 , η_2 , η_3 , a_0 , a_1 , a_2 , K , and C_1 in Figure 18.

Note that the plots from Figures 7, 11 and 15 present an increasing pattern, and they tend toward zero. In Figure 11, the plot appears only tending toward zero, but, in Figures 7 and 15, a clear tendency toward zero behavior is observed. Furthermore, the graph for R as a quadratic function, i.e., Figure 7, and R as a linear function, i.e., Figure 15, show a similar pattern; however, R as an exponential pattern, i.e., Figure 11, shows a significantly different form. Note that, in all three graphs, F increases with an increase in the radius after a certain value of the radius.

In Figures 8 and 16, we represent F for R as a function of quadratic form and linear form of radius, respectively. Though F eventually started with a decreasing pattern, it kept increasing for the increasing radius. Furthermore, these two graphs show a similar pattern. Figure 12 represents F for R as an exponential function of radius. This graph shows a clear ascending shape and a significantly different pattern from the other two.

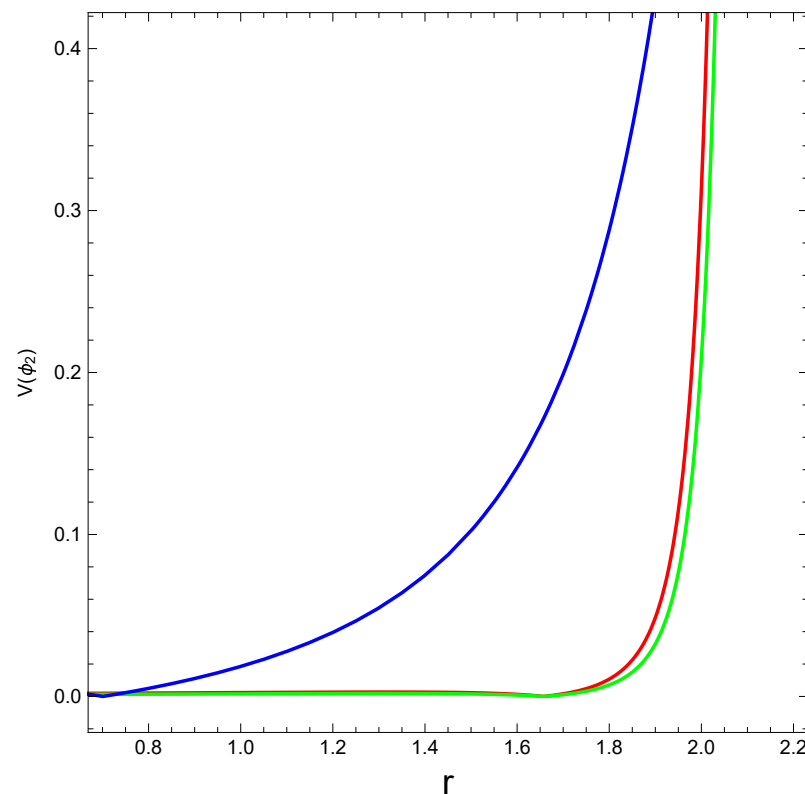


Figure 18. Solution of the scalar potential for R adopted as a linear function of radius. The evolution of the scalar potential $V(\phi_2)$ is obtained by comparing Equation (8) and Equation (32). We have fixed the values of $a_0, a_1, a_2, K,$ and C_1 . The red, green, and blue lines correspond to small perturbations of $\lambda_0, \Psi_0, \eta_1, \eta_2,$ and $\eta_3,$ respectively.

Figures 9, 13 and 17 represent the scalar potential $V(\phi_2)$ for three different form of functions of R . Figures 9 and 17 demonstrate R as a quadratic and linear function of the radius, and these two graphical representations show a similar pattern. These two graphs converge to zero. Figure 13 represents the exponential function of radius, and this graph tends to zero. All three graphs present an ascending pattern, i.e., the scalar potential converges to zero near the center, and, in due course, it keeps increasing with the increasing rate of the radius.

For Figures 10, 14 and 18, an ascending pattern has been observed as well. Figure 10 represents R as a quadratic function of the radius. Figure 14 shows R as an exponential function of the radius, and Figure 18 represents R as a linear function of the radius. All three graphical representation show a progressive pattern that implies the potential will keep increasing for the particle going away from the core. Here, the three graphs have an apparent convergence to zero for a small value of the radial coordinate. So, the potential will tend to zero whenever a particle is very near to the core.

4. Viable $f(R)$ Gravity Models

Several viable $f(R)$ gravity models are adopted based on the following conditions [40]: (a) positive effect for gravitational coupling, (b) stable effect on cosmological perturbation [54], (c) in a large curvature regime, asymptotic behavior should be preserved to standard Λ Cold Dark Matter (Λ CDM), (d) late-time de-Sitter point should be stable [55], and (e) solar system constraints [56] should be satisfied as well. After several literature studies, some popular viable models have been adopted for the evolution of the scalar potential. Such models are: (a) Hu–Sawicki [57], (b) Starobinsky [58], (c) Tsujikawa [59], and (d) the exponential gravity [60–62]. All these models are explicitly described as follows.

4.1. Hu–Sawicki Model

This $f(R)$ gravity model, in particular, is not designed with a cosmological constant even though it satisfies cosmological and solar system constraints until a certain parametric space limit. The minimization of the potential for the scalar degree of freedom $f_R = df(R)/dR$ is possible in this model for a high curvature value for the Ricci scalar R . The cosmological and Local Gravity Constraints are preserved in this model as well:

$$f(R) = R - \frac{c_1 R_{HS} \left(\frac{R}{R_{HS}}\right)^p}{c_2 \left(\frac{R}{R_{HS}}\right)^p + 1}, \tag{40}$$

where c_1, c_2, R_{HS} , and p are positive and R_{HS} denote the order of present the Ricci Scalar. For the scalar potential, we need to compare Equation (32) and Equation (40). We have

$$F = \frac{\partial f}{\partial R} = 1 - \frac{c_1 p \left(\frac{R}{R_{HS}}\right)^{-1+p}}{1 + c_2 \left(\frac{R}{R_{HS}}\right)^p} + \frac{c_1 c_2 p \left(\frac{R}{R_{HS}}\right)^{-1+2p}}{\left(1 + c_2 \left(\frac{R}{R_{HS}}\right)^p\right)^2}, \tag{41}$$

$$V(\phi_2) = \frac{1}{2} \left(-R + R \left(1 - \frac{c_1 p \left(\frac{R}{R_{HS}}\right)^{-1+p}}{1 + c_2 \left(\frac{R}{R_{HS}}\right)^p} + \frac{c_1 c_2 p \left(\frac{R}{R_{HS}}\right)^{-1+2p}}{\left(1 + c_2 \left(\frac{R}{R_{HS}}\right)^p\right)^2} \right) + \frac{c_1 \left(\frac{R}{R_{HS}}\right)^p R_{HS}}{1 + c_2 \left(\frac{R}{R_{HS}}\right)^p} \right). \tag{42}$$

Using $c_1 = 2, c_2 = 3$ of the graphical representation of F is provided in Figure 19, Figure 20, Figure 21, and $V(\phi_2)$ in Figure 22, Figure 23, and Figure 24, respectively.

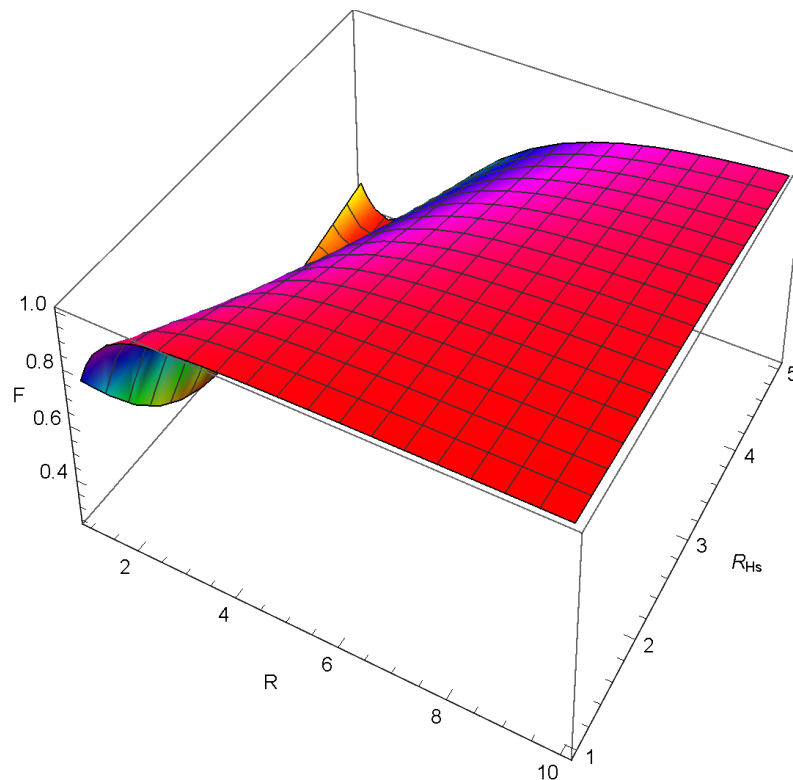


Figure 19. Solution of $F(R)$ for $p = 2$. The evolution of the partial derivative of $f(R)$ is obtained using Equations (33) and (41).

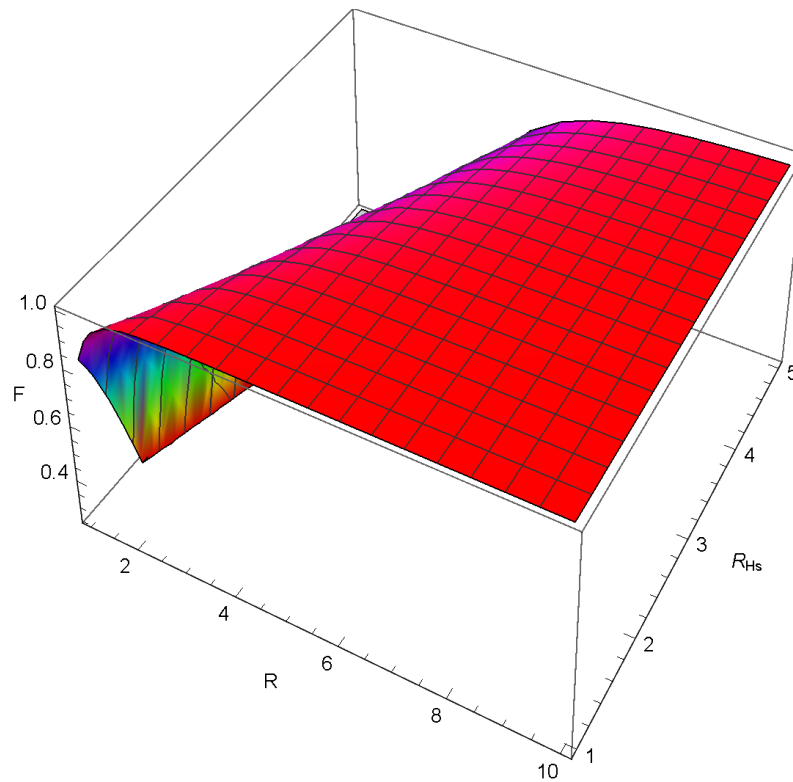


Figure 20. Solution of $F(R)$ for $p = 3$. The evolution of the partial derivative of $f(R)$ is obtained using Equations (33) and (41).

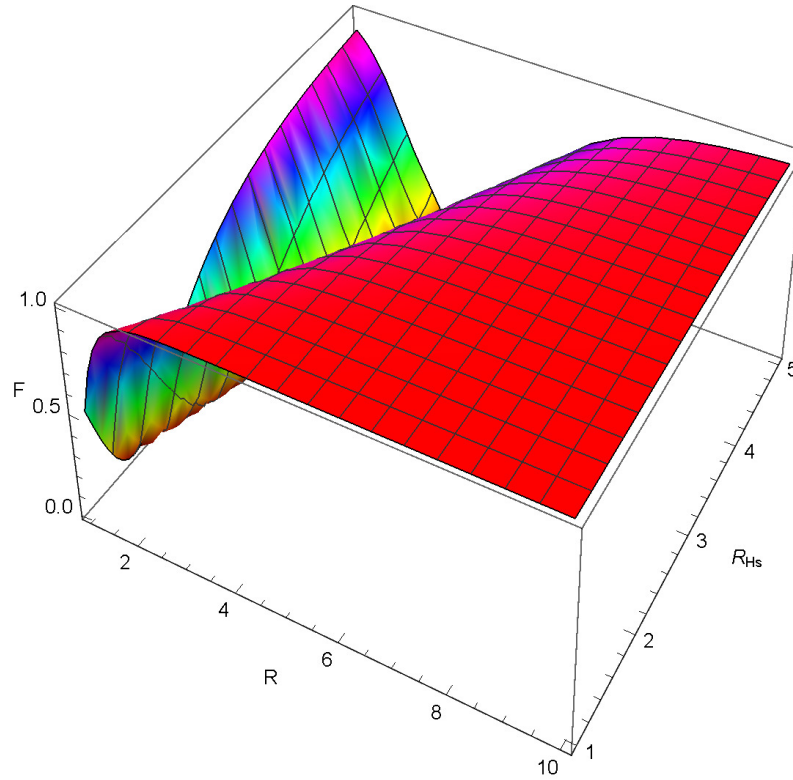


Figure 21. Solution of $F(R)$ for $p = 4$. The evolution of the partial derivative of $f(R)$ is obtained using Equations (33) and (41).

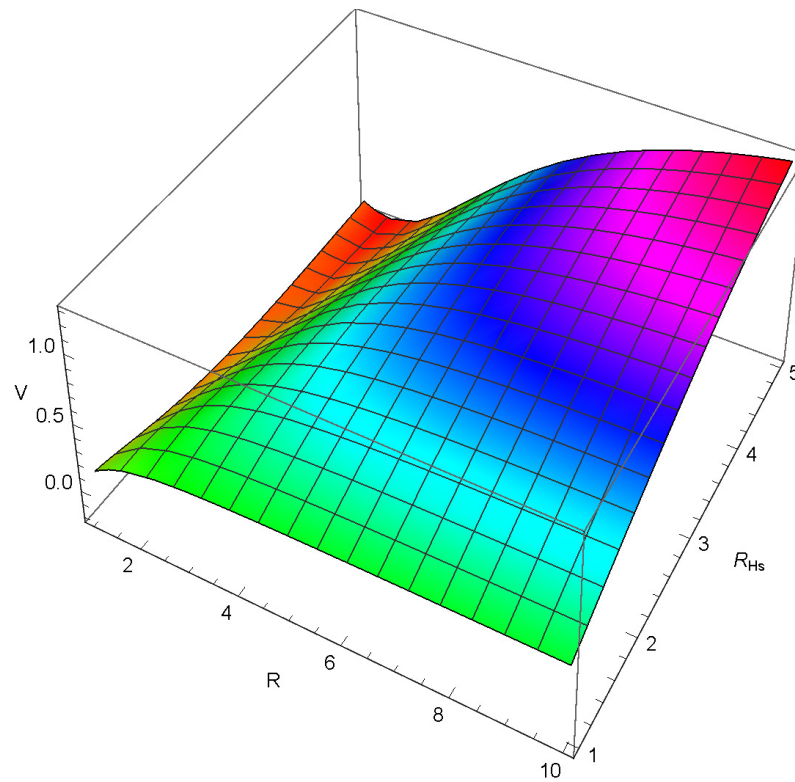


Figure 22. Solution of $V(\phi_2)$ for $p = 2$. The evolution of $V(\phi_2)$ is obtained using Equations (32) and (42).

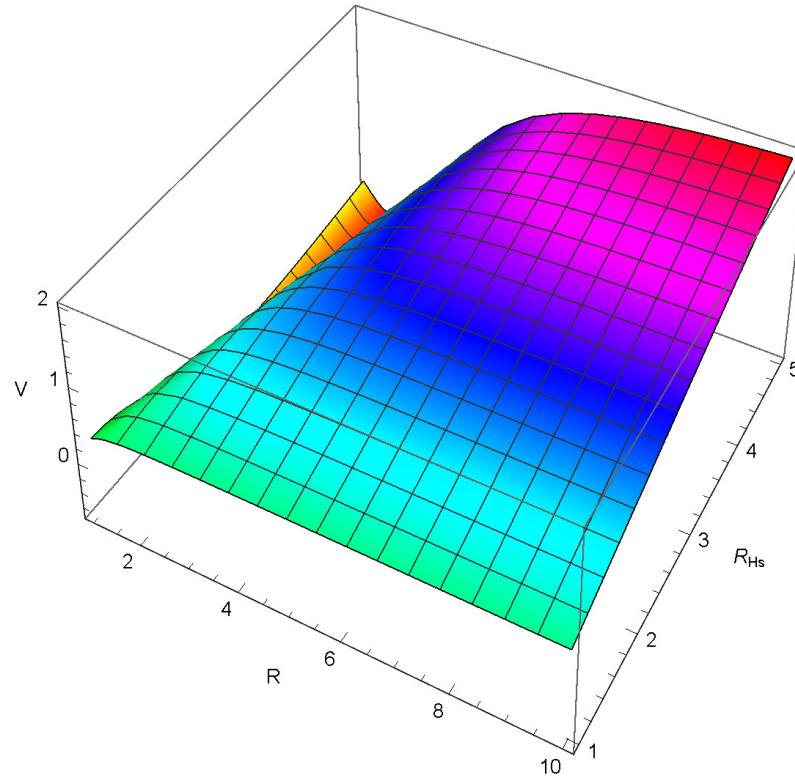


Figure 23. Solution of $V(\phi_2)$ for $p = 3$. The evolution of $V(\phi_2)$ is obtained using Equations (32) and (42).

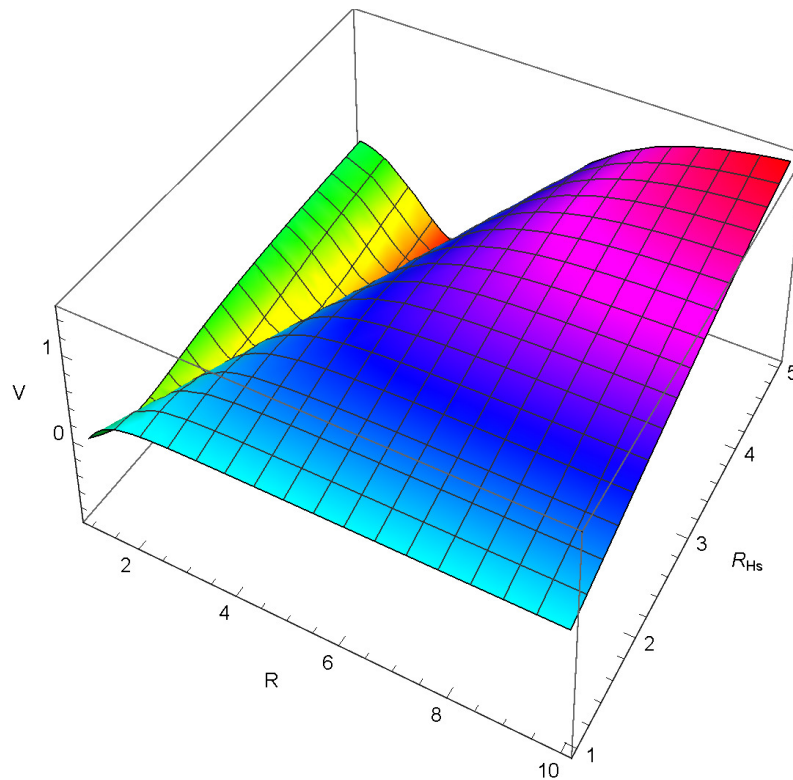


Figure 24. Solution of $V(\phi_2)$ for $p = 4$. The evolution of $V(\phi_2)$ is obtained using Equations (32) and (42).

Here, the scalar potential shows a clear convergence to zero with the increase in the Ricci scalar (R).

4.2. Starobinsky Model

The Starobinsky Model is a three-parametric form $f(R)$ model provided by

$$f(R) = R + \lambda R_S \left(\left(1 + \frac{R^2}{R_S^2} \right)^{-n} - 1 \right), \tag{43}$$

where $n, \lambda > 0$, and R_S is the order of the presently observed effective cosmological constant. Here, $f(0) = 0$ implies the ‘cosmological constant’ vanishes in flat space–time. For a sufficiently large value of the parameter n , this model passes the laboratory and solar system tests of gravity. Though new restrictions may be added due to the analysis of radiation from double pulsar. We can easily evaluate the scalar potential $V(\phi_2)$ by comparing Equation (32) with Equation (43):

$$F = \frac{\partial f}{\partial R} = 1 - \frac{2nR \left(1 + \frac{R^2}{R_S^2} \right)^{-1-n} \lambda}{R_S}, \tag{44}$$

$$V(\phi_2) = \frac{1}{2} \left(-R - \left(-1 + \left(1 + \frac{R^2}{R_S^2} \right)^{-n} \right) R_S \lambda + R \left(1 - \frac{2nR \left(1 + \frac{R^2}{R_S^2} \right)^{-1-n} \lambda}{R_S} \right) \right). \tag{45}$$

Adopting the cosmological constant equal to 20, the graphical representation of F is provided in Figures 25–27 and of $V(\phi_2)$ in Figures 28–30.

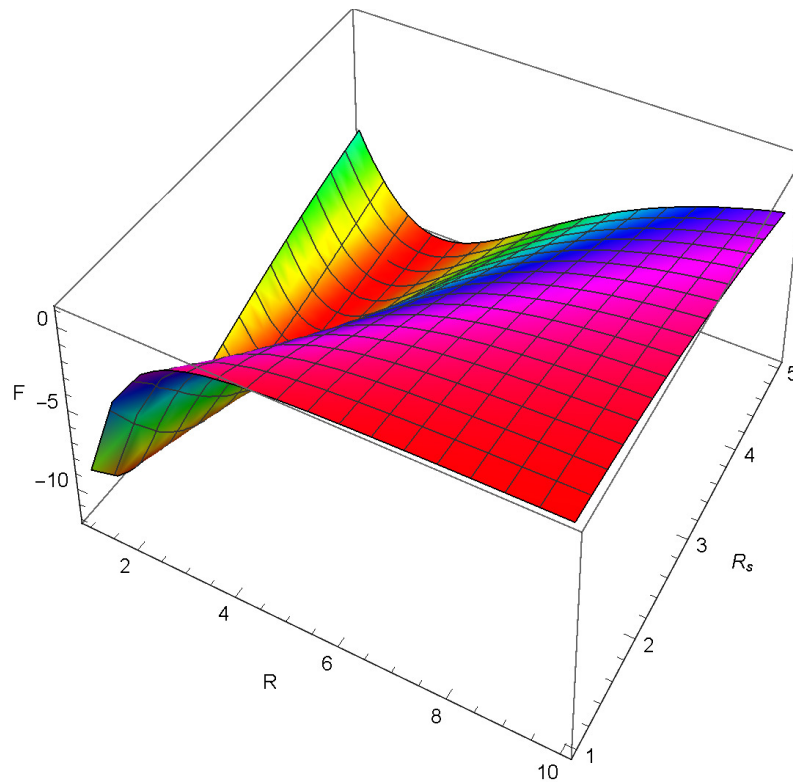


Figure 25. Solution of $F(R(r))$ for $n = 1$. The evolution of partial derivative of $f(R)$ is obtained using Equations (33) and (44).

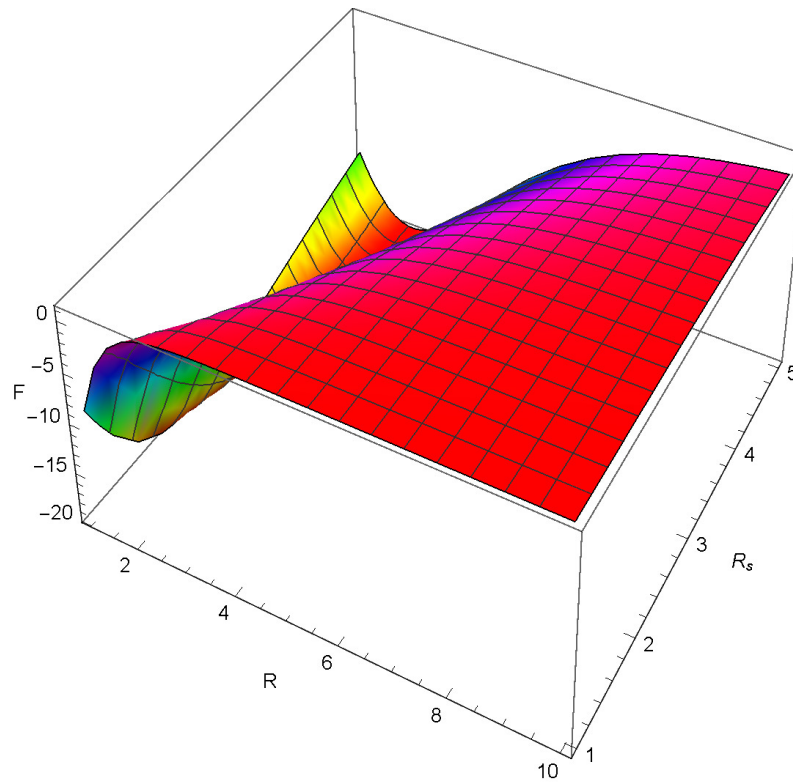


Figure 26. Solution of $F(R(r))$ for $n = 2$. The evolution of partial derivative of $f(R)$ is obtained using Equations (33) and (44).

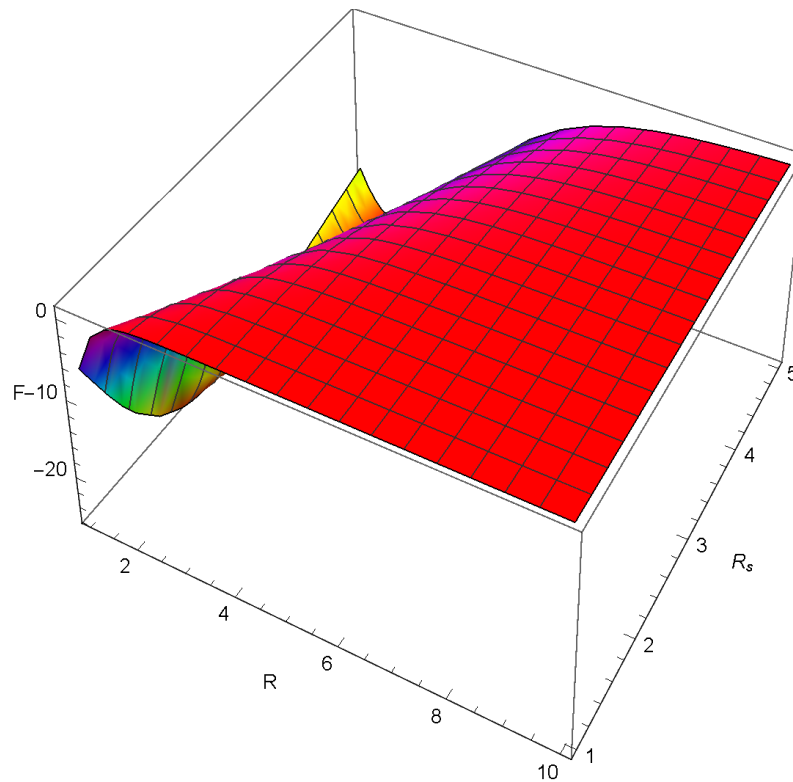


Figure 27. Solution of $F(R(r))$ for $n = 3$. The evolution of partial derivative of $f(R)$ is obtained using Equations (33) and (44).

The scalar potential for this model is:

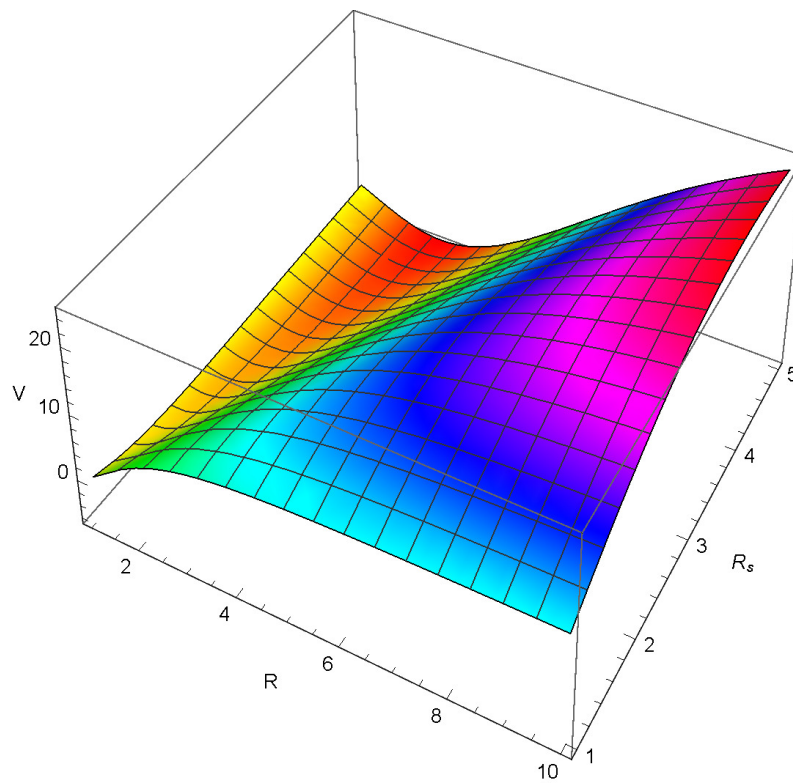


Figure 28. Solution of $V(\phi_2)$ for $n = 1$. The evolution of $V(\phi_2)$ is obtained using Equations (32) and (45).

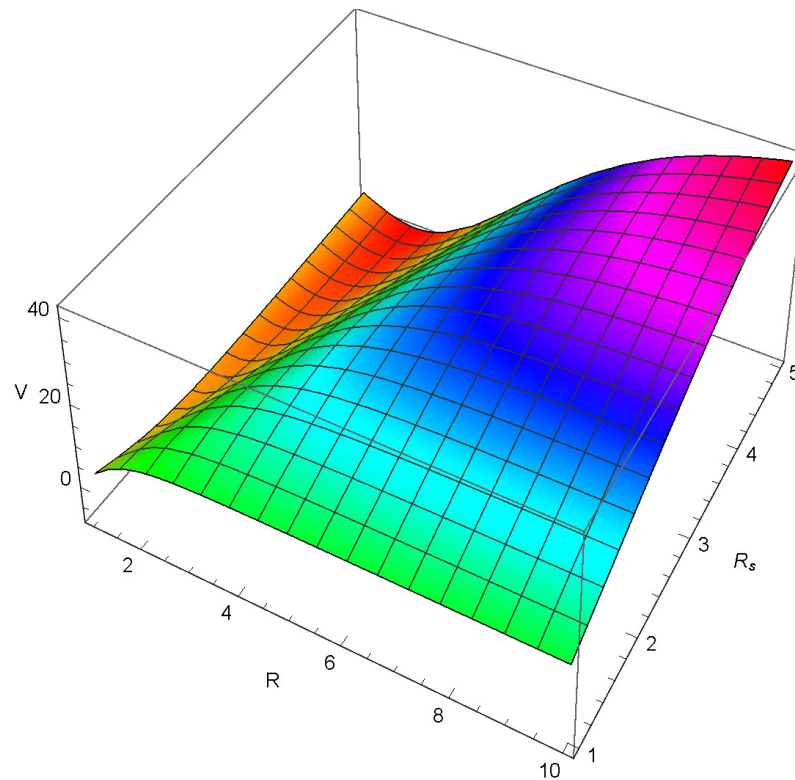


Figure 29. Solution of $V(\phi_2)$ for $n = 2$. The evolution of $V(\phi_2)$ is obtained using Equations (32) and (45).

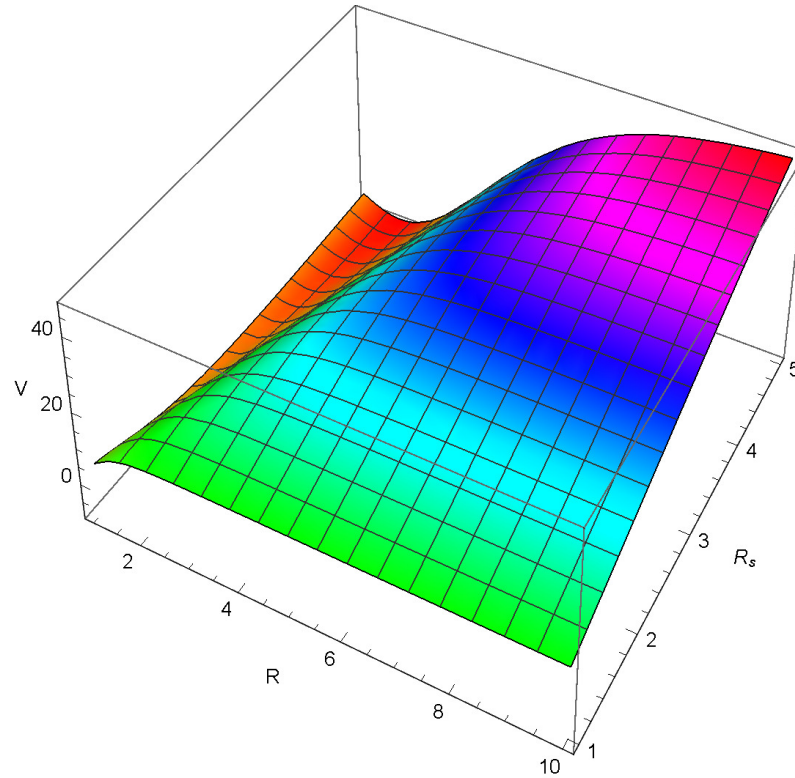


Figure 30. Solution of $V(\phi_2)$ for $n = 3$. The evolution of $V(\phi_2)$ is obtained using Equations (32) and (45).

The scalar potential converges to zero as the Ricci scalar (R) increases.

4.3. Tsujikawa Model

Another important viable $f(R)$ gravity model that satisfies the required condition is

$$f(R) = R - \mu R_T \tanh\left(\frac{R}{R_T}\right), \tag{46}$$

where $\mu (>0)$ and $R_T (>0)$ are constant parameters. Now, to find the scalar potential $V(\phi_2)$ in Equation (32) we need to compare with Equation (46). Thus,

$$F = \frac{\partial f}{\partial R} = 1 - \mu \operatorname{sech}^2\left(\frac{R}{R_T}\right), \tag{47}$$

$$V(\phi_2) = \frac{1}{2} \left(-R + R \left(1 - \mu \operatorname{sech}^2\left(\frac{R}{R_T}\right) \right) + R_T \mu \operatorname{Tanh}\left(\frac{R}{R_T}\right) \right). \tag{48}$$

Figure 31 represents the partial derivative of $F(R)$ and shows a decaying pattern, and Figure 32 represents the scalar potential and shows a convergence to zero. Thus, it can be concluded that, for small values of the Ricci scalar (R), the scalar potential tends to be zero. When R is increasing, the scalar potential also increases with definite steps.

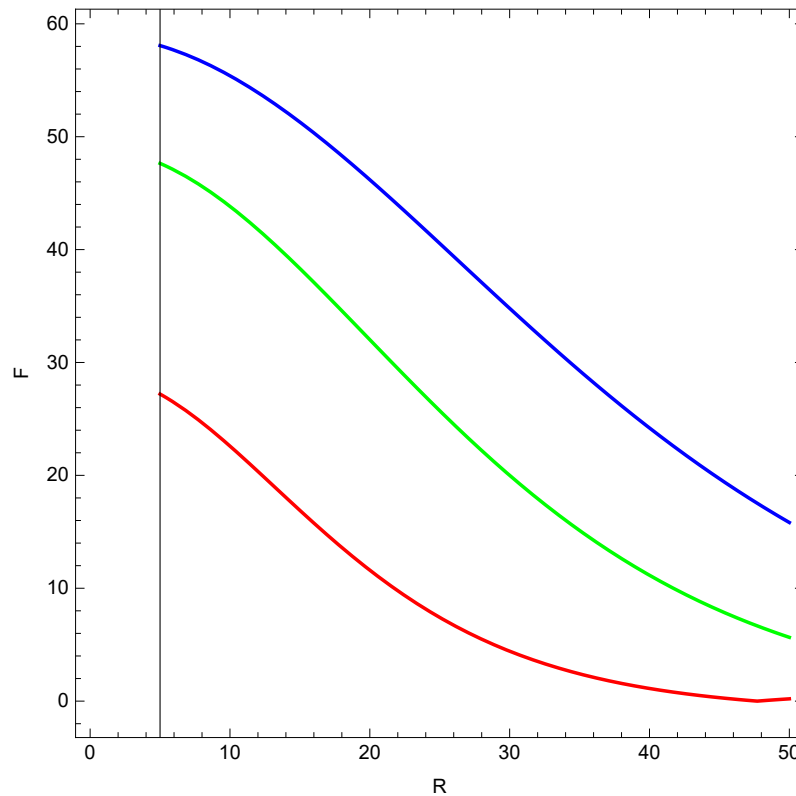


Figure 31. The evolution of F is obtained using Equations (33) and (46). The red, green, and blue lines correspond to small perturbations of R_T and μ , respectively.

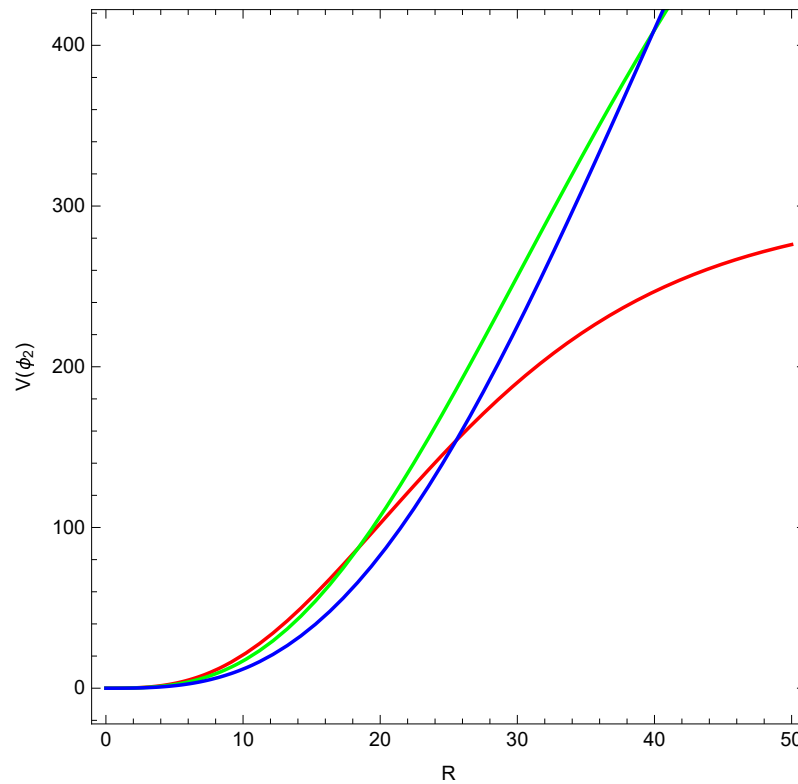


Figure 32. The evolution of $V(\phi_2)$ is obtained using Equations (32) and (46). The red, green, and blue lines correspond to small perturbations of R_T and μ , respectively.

4.4. The Exponential Gravity Model

We have

$$f(R) = R - \beta R_E \left(1 - e^{-\frac{R}{R_E}}\right), \tag{49}$$

where β and R_E are parameters. To find the scalar potential $V(\phi_2)$, we compare Equation (49) with Equation (32) and we obtain

$$F = \frac{\partial f}{\partial R} = 1 - e^{-\frac{R}{R_E}} \beta, \tag{50}$$

$$V(\phi_2) = \frac{1}{2} \left(-R + \left(1 - e^{-\frac{R}{R_E}}\right) R_E \beta + R \left(1 - e^{-\frac{R}{R_E}} \beta\right) \right). \tag{51}$$

For different values of R_E , the graphical forms of representations F and $V(\phi_2)$ are presented in Figure 33 and Figure 34, respectively.

Figure 33 represents the partial derivative of $F(R)$, and this shows a decaying pattern. Figure 34 represents the scalar potential $V(\phi_2)$ and shows a clear convergence to zero. We concluded that, for small values of the Ricci scalar (R), the scalar potential tends to zero. When R increases, the scalar potential will also increase with definite steps.

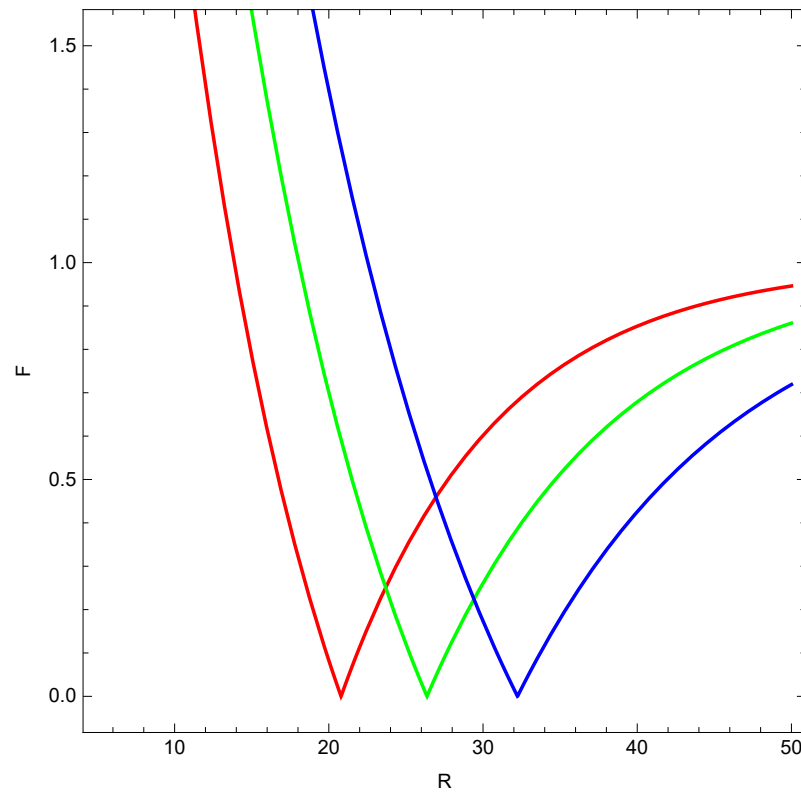


Figure 33. The evolution of F is obtained by Equations (33) and (49). The red, green, and blue lines correspond to small perturbations of R_E and β , respectively.

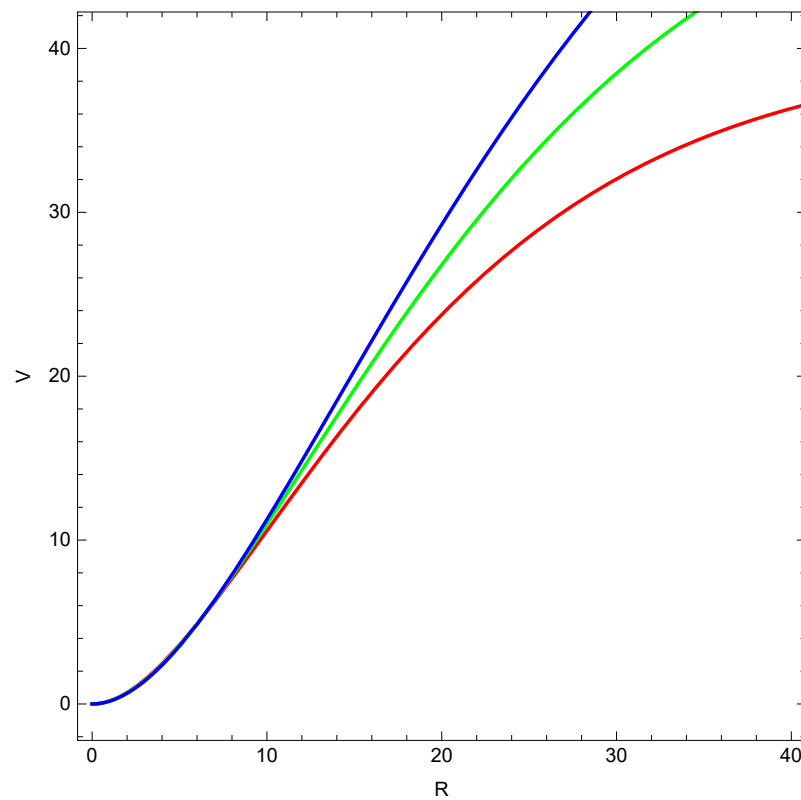


Figure 34. The evolution of $V(\phi_2)$ is obtained by Equations (32) and (49). The red, green, and blue lines correspond to small perturbations of R_E and β , respectively.

5. Conclusions

In this work, we have discussed Neutron Stars in the $f(R)$ gravity framework for different models. Firstly, we have considered the TOV equation for the $f(R)$ gravity framework [41], and we obtained two higher order differential equations concerning λ (function of radial coordinate) and ψ (function of radial coordinate). The differential equations are presented in Equations (7) and (8), which involve two non-linear functions of the radial coordinate r as the dependent variables and r as the independent variable. Here, we have also used the Polytropic Gas model [47] in the form of Equation (10) to compare with the TOV form and observed the evolution of $f(R)$. Without assuming any specific form of the $f(R)$ gravity models, we have expressed the Ricci scalar R as a function of the radial coordinate r , in some arbitrary form such as the quadratic form, exponential form, and linear form. In Section 2, for three different radial forms, we obtained a set of three different solutions for $f(R(r))$ for λ (function of the radial coordinate r) [compared with Equation (7)] and with respect to ψ (function of the radial coordinate r) [compared with Equation (8)] as well. We have presented the graphs of the solution of $f(R)$ in Figures 1, 3, 5, 2, 4 and 6, which show an ascending pattern with an increase in the rate of the radius. Furthermore, all the sets of solutions tend to converge to zero. In Section 3, we have applied the BD-theory [51], which is an equivalent theory of $f(R)$ gravity. Still, the BD-theory introduced a new scalar field ϕ_2 with the scalar potential $V(\phi_2)$. In this section, three arbitrary functions of the radius have expressed the Ricci scalar (R) and, with the aid of that, the partial derivative of $f(R(r))$ and the scalar potential V have been derived for λ and ψ . Figures 7, 11 and 15 represent the graphical representation of $F(R)$ [partial derivative of $f(R)$] with respect to λ and Figures 8, 12 and 16 represent $F(R)$ [partial derivative of $f(R)$] considering ψ for R as quadratic, exponential, and linear form, respectively. All the partial derivatives show an increasing pattern for the radius. Although, Figures 8 and 16 show a decrease in the early stage, they also show an increasing pattern. In the next phase, we observed the evolution of the scalar potential $V(\phi_2)$ with respect to λ and ψ for different forms proposed earlier. Figures 9, 13, and 17 represent V for R as quadratic, exponential, and linear forms with respect to λ . Figures 9 and 17 have a clear indication of convergence to zero, whereas Figure 13 tends to zero for smaller values of the radius, i.e., for R being a function of a quadratic and linear function of the radius, the potential will tend to zero near the core of the NS. Figures 10, 14 and 18 show V with respect to ψ . Here, all three representations converge to zero near the star's core. In Section 4, we have compared four important viable models: (a) Hu–Sawicki model [57], (b) Starobinsky model [58], (c) Tsujikawa model [59], and (d) Exponential Gravity model [60–62]. The (a) Hu–Sawicki model and (b) Starobinsky model contain the power form of the Ricci scalar R in $f(R)$. For three different power values, the partial derivative of $f(R)$ and the scalar potential V have been demonstrated. In both models, the scalar potential shows a convergence pattern to zero. At the same time, the (c) Tsujikawa model and (d) Exponential Gravity model have different parameters of the Ricci scalar R in $f(R)$. In these two models, the convergence to zero for different parametric values dominates the graphs. For the (a) Hu–Sawicki model, Figures 33, 34 and 25 show the scalar potential. For the (b) Starobinsky model, Figures 28, 29 and 30 present the evolution of $V(\phi_2)$. For the (c) Tsujikawa model, Figure 21 demonstrates the evolution of the scalar potential, and, for the (d) Exponential Gravity model, Figure 23 shows the development of the scalar potential for R . Our proposed models (a) quadratic form, (b) exponential form, (c) linear form, and the viable models of the $f(R)$ gravity show similar a type of evolution for the scalar potential $V(\phi_2)$.

While concluding, let us mention the outcomes of our work in connection with some relevant studies [44,51] where the authors studied \mathcal{M} - \mathcal{R} diagram of NS for $f(R)$ gravity for some viable models. Nevertheless, we have demonstrated the scalar potential under BD-theory of NS for some viable models from the influence of K. Bamba's work [40]. Moreover, we have demonstrated the consequences of the (a) quadratic form, (b) exponential form, and (c) linear form of the Ricci scalar R in the current astrophysical setting.

In the context of this extensive study, it must be mentioned that Einstein gravity is a very powerful theory because there does not seem to be much that is not described in it. As a consequence, one would expect to find its possible corrections to be very small. Then, the corrections for stellar systems such as neutron stars might be significantly small. Here, the question about the applicability of $f(R)$ gravity to neutron stars arises. In [50], it was demonstrated that, under the purview of $f(R)$ gravity, it is possible to have an increase in the upper limit of neutron star mass and, therefore, realistic star configurations can be realized through the appropriate equation of state. Another noteworthy work in this context is [63], which investigated the causal limit of the maximum mass of stars in cosmological settings of $f(R)$ gravity and concluded with the secondary component of the compact binary GW190814, possibly a neutron star. In the light of these works, we proposed to extend our study in future to rapidly rotating neutron stars with the other forms of modified gravity, and to demonstrate the causal limit of the maximum mass of the stars. While concluding, let us comment on the outcomes of the present study with respect to some noteworthy works. In [64], the authors obtained the interior solutions of exotic stars constituted of dark energy, considering the presence of anisotropies and adopting the extended Chaplygin gas equation of state. The study [65] reported properties of strange stars under the purview of an extreme SQSB40 MIT bag model, and assuming, for quark matter, a linear EoS. In [66], the authors have examined an EOS of a strange matter phase for non-rotating quark stars and the pressure of anisotropy present in that context. From [67], we observe that the authors have studied the gravitational decoupling under the purview of anisotropic domains extended by four anisotropic models. Another relevant work in the context of the current study is [68], where $f(R, T)$ gravity was adopted to demonstrate the analytic relativistic anisotropic spherical solutions; in it, the relationship between the effective pressure and effective density was established. Given the studies mentioned above, the aim of the authors of the current work was to extend their study to other forms of modified gravity including $f(R, T)$ gravity and to provide a deeper look inside into the strange quark stars under the purview of an MIT Bag model.

Author Contributions: All authors contributed equally to this paper. All authors have read and agreed to the published version of the manuscript.

Funding: This research received no external funding.

Data Availability Statement: The work does not involve any data.

Acknowledgments: The authors are thankful to the anonymous reviewers for their insightful and supportive comments.

Conflicts of Interest: The authors declare no conflict of interest.

References

1. Branch, D. Type Ia supernovae and the Hubble constant. *Annu. Rev. Astron. Astrophys.* **1998**, *36*, 17–55. [[CrossRef](#)]
2. Riess, A.G.; Filippenko, A.V.; Challis, P.; Clocchiatti, A.; Diercks, A.; Garnavich, P.M.; Gillil, R.L.; Hogan, C.J.; Jha, S.; Kirshner, R.P.; et al. Observational evidence from supernovae for an accelerating universe and a cosmological constant. *Astron. J.* **1998**, *116*, 1009. [[CrossRef](#)]
3. Perlmutter, S.; Aldering, G.; Goldhaber, G.; Knop, R.A.; Nugent, P.; Castro, P.G.; Deustua, S.; Fabbro, S.; Goobar, A.; Groom, D.E.; et al. Measurements of Ω and Λ from 42 high-redshift supernovae. *Astrophys. J.* **1999**, *517*, 565. [[CrossRef](#)]
4. Caldwell, R.R.; Doran, M. Cosmic microwave background and supernova constraints on quintessence: Concordance regions and target models. *Phys. Rev. D* **2004**, *69*, 103517. [[CrossRef](#)]
5. Koivisto, T.; Mota, D.F. Dark energy anisotropic stress and large scale structure formation. *Phys. Rev. D* **2006**, *73*, 083502. [[CrossRef](#)]
6. Colless, M.; Dalton, G.; Maddox, S.; Sutherland, W.; Norberg, P.; Cole, S.; Bland-Hawthorn, J.; Bridges, T.; Cannon, R.; Collins, C.; et al. The 2df galaxy redshift survey: Spectra and redshifts. *Mon. Not. R. Astron. Soc.* **2001**, *328*, 1039–1063. [[CrossRef](#)]
7. Copeland, E.J.; Sami, M.; Tsujikawa, S. Dynamics of dark energy. *Int. J. Mod. Phys. D* **2006**, *15*, 1753–1935. [[CrossRef](#)]
8. Bamba, K.; Capozziello, S.; Nojiri, S.I.; Odintsov, S.D. Dark energy cosmology: The equivalent description via different theoretical models and cosmography tests. *Astrophys. Space Sci.* **2012**, *342*, 155–228. [[CrossRef](#)]

9. Suzuki, N.; Rubin, D.; Lidman, C.; Aldering, G.; Amanullah, R.; Barbary, K.; Barrientos, L.F.; Botyanszki, J.; Brodwin, M.; Connolly, N.; et al. The Hubble Space Telescope cluster supernova survey. V. Improving the dark-energy constraints above $z > 1$ and building an early-type-hosted supernova sample. *Astrophys. J.* **2012**, *746*, 85. [[CrossRef](#)]
10. Caldwell, R.R.; Kamionkowski, M. The physics of cosmic Acceleration. *Annu. Rev. Nucl. Part. Sci.* **2009**, *59*, 397–429. [[CrossRef](#)]
11. Zhang, H.; Zhu, Z.H. Interacting chaplygin gas. *Phys. Rev. D* **2006**, *73*, 043518. [[CrossRef](#)]
12. Bilić, N.; Tupper, G.B.; Viollier, R.D. Unification of dark matter and dark energy: The inhomogeneous Chaplygin gas. *Phys. Lett. B* **2002**, *535*, 17–21. [[CrossRef](#)]
13. Myung, Y.S. Holographic principle and dark energy. *Phys. Lett. B* **2005**, *610*, 18–22. [[CrossRef](#)]
14. Karami, K.; Ghaffari, S. The generalized second law of thermodynamics for the interacting polytropic dark energy in non-flat FRW universe enclosed by the apparent horizon. *Phys. Lett. B* **2010**, *688*, 125–128. [[CrossRef](#)]
15. Karami, K.; Ghaffari, S.; Fehri, J. Interacting polytropic gas model of phantom dark energy in non-flat universe. *Eur. Phys. J. C* **2009**, *64*, 85–88. [[CrossRef](#)]
16. Bamba, K.; Matsumoto, J.; Nojiri, S.I. Cosmological perturbations in the k-essence model. *Phys. Rev. D* **2012**, *85*, 084026. [[CrossRef](#)]
17. Nojiri, S.I.; Odintsov, S.D. Introduction to modified gravity and gravitational alternative for dark energy. *Int. J. Geom. Methods Mod. Phys.* **2007**, *4*, 115–145. [[CrossRef](#)]
18. Sotiriou, T.P.; Faraoni, V. $f(R)$ theories of gravity. *Rev. Mod. Phys.* **2010**, *82*, 451.
19. Nojiri, S.I.; Odintsov, S.D. Unifying phantom inflation with late-time acceleration: Scalar phantom–non-phantom transition model and generalized holographic dark energy. *Gen. Relativ. Gravit.* **2006**, *38*, 1285–1304. [[CrossRef](#)]
20. Nojiri, S.; Odintsov, S.D. Modified Gauss–Bonnet theory as gravitational alternative for dark energy. *Phys. Lett. B* **2005**, *631*, 1–6. [[CrossRef](#)]
21. Bergmann, P.G. Comments on the scalar-tensor theory. *Int. J. Theor. Phys.* **1968**, *1*, 25–36. [[CrossRef](#)]
22. Aldrovandi, R.; Pereira, J.G. Why to study teleparallel gravity. In *Teleparallel Gravity*; Springer: Dordrecht, The Netherlands, 2013; pp. 179–186.
23. Sharif, M.; Rani, S. Entropy corrected holographic dark energy $f(T)$ gravity model. *Mod. Phys. Lett. A* **2014**, *29*, 1450015. [[CrossRef](#)]
24. Karami, K.; Abdolmaleki, A. $f(T)$ modified teleparallel gravity as an alternative for holographic and new agegraphic dark energy models. *Res. Astron. Astrophys.* **2013**, *13*, 757. [[CrossRef](#)]
25. Setare, M.R.; Darabi, F. Power-law solutions in $f(T)$ gravity. *Gen. Relativ. Gravit.* **2012**, *44*, 2521–2527. [[CrossRef](#)]
26. Karami, K.; Khaledian, M.S. Polytropic and Chaplygin $f(R)$ -gravity models. *Int. J. Mod. Phys. D* **2012**, *21*, 1250083. [[CrossRef](#)]
27. Güver, T.; Erkoca, A.E.; Reno, M.H.; Sarcevic, I. On the capture of dark matter by neutron stars. *J. Cosmol. Astropart. Phys.* **2014**, *2014*, 13. [[CrossRef](#)]
28. Linder, E.V. Exponential gravity. *Phys. Rev. D* **2009**, *80*, 123528. [[CrossRef](#)]
29. Elizalde, E.; Nojiri, S.; Odintsov, S.D.; Sebastiani, L.; Zerbini, S. Nonsingular exponential gravity: A simple theory for early-and late-time accelerated expansion. *Phys. Rev. D* **2011**, *83*, 086006. [[CrossRef](#)]
30. Astashenok, A.V.; Capozziello, S.; Odintsov, S.D. Further stable neutron star models from $f(R)$ gravity. *J. Cosmol. Astropart. Phys.* **2013**, *2013*, 40. [[CrossRef](#)]
31. Haensel, P.; Zdunik, J.L.; Douchin, F. Equation of state of dense matter and the minimum mass of cold neutron stars. *Astron. Astrophys.* **2002**, *385*, 301–307. [[CrossRef](#)]
32. Chandrasekhar, S. The maximum mass of ideal white dwarfs. *Astrophys. J.* **1931**, *74*, 81. [[CrossRef](#)]
33. Oppenheimer, J.R. Volkoff. *Phys. Rev.* **1939**, *55*, 374. [[CrossRef](#)]
34. O’Hanlon, J. Intermediate-range gravity: A generally covariant model. *Physical Rev. Lett.* **1972**, *29*, 137. [[CrossRef](#)]
35. Chiba, T. $1/R$ gravity and scalar-tensor gravity. *Phys. Lett. B* **2003**, *575*, 1–3. [[CrossRef](#)]
36. Fujii, Y.; Maeda, K.I. *The Scalar-Tensor Theory of Gravitation*; Cambridge University Press: Cambridge, UK, 2003.
37. Khoury, J.; Weltman, A. Chameleon cosmology. *Phys. Rev. D* **2004**, *69*, 044026. [[CrossRef](#)]
38. Tsujikawa, S.; Uddin, K.; Mizuno, S.; Tavakol, R.; Yokoyama, J.I. Constraints on scalar-tensor models of dark energy from observational and local gravity tests. *Phys. Rev. D* **2008**, *77*, 103009. [[CrossRef](#)]
39. De Felice, A.; Tsujikawa, S. $f(R)$ theories. *Living Rev. Relativ.* **2010**, *13*, 1–161. [[CrossRef](#)]
40. Bamba, K.; Geng, C.Q.; Lee, C.C. Generic feature of future crossing of phantom divide in viable $f(R)$ gravity models. *J. Cosmol. Astropart. Phys.* **2010**, *2010*, 001. [[CrossRef](#)]
41. Capozziello, S.; De Laurentis, M. Extended theories of gravity. *Phys. Rep.* **2011**, *509*, 167–321. [[CrossRef](#)]
42. Nojiri, S.I.; Odintsov, S.D. Unified cosmic history in modified gravity: From $F(R)$ theory to Lorentz non-invariant models. *Phys. Rep.* **2011**, *505*, 59–144. [[CrossRef](#)]
43. Capozziello, S.; Francaviglia, M. Extended theories of gravity and their cosmological and astrophysical applications. *Gen. Relativ. Gravit.* **2008**, *40*, 357–420. [[CrossRef](#)]
44. Astashenok, A.V.; Capozziello, S.; Odintsov, S.D.; Oikonomou, V.K. Extended gravity description for the GW190814 supermassive neutron star. *Physics Letters B* **2020**, *811*, 135910. [[CrossRef](#)]
45. Weinberg, S. *Gravitation and Cosmology*; John Wiley & Sons Inc.: New York, NY, USA, 1972.
46. Astashenok, A.V.; Capozziello, S.; Odintsov, S.D. Nonperturbative models of quark stars in $f(R)$ gravity. *Phys. Lett. B* **2015**, *742*, 160–166. [[CrossRef](#)]

47. Chattopadhyay, S.; Jawad, A.; Rani, S. Holographic polytropic gravity models. *Adv. High Energy Phys.* **2015**, *2015*, 798902. [[CrossRef](#)]
48. Astashenok, A.V.; Capozziello, S.; Odintsov, S.D. Maximal neutron star mass and the resolution of the hyperon puzzle in modified gravity. *Phys. Rev. D* **2014**, *89*, 103509. [[CrossRef](#)]
49. Faber, J.A.; Grandclément, P.; Rasio, F.A. Mergers of irrotational neutron star binaries in conformally flat gravity. *Phys. Rev. D* **2004**, *69*, 124036. [[CrossRef](#)]
50. Cooney, A.; DeDeo, S.; Psaltis, D. Neutron stars in $f(R)$ gravity with perturbative constraints. *Phys. Rev. D* **2010**, *82*, 064033.
51. Kase, R.; Tsujikawa, S. Neutron stars in $f(R)$ gravity and scalar-tensor theories. *J. Cosmol. Astropart. Phys.* **2019**, *2019*, 054. [[CrossRef](#)]
52. Branss, C.; Dicke, R.H. Mach's principle and a relativistic theory of gravitation. *Phys. Rev.* **1961**, *124*, 925. [[CrossRef](#)]
53. Clifton, T.; Ferreira, P.G.; Padilla, A.; Skordis, C. Modified gravity and cosmology. *Phys. Rep.* **2012**, *513*, 1–189.
54. Faraoni, V. Matter instability in modified gravity. *Phys. Rev. D* **2006**, *74*, 104017. [[CrossRef](#)]
55. Starobinsky, A.A. *Classical Quantum Gravity* **4**, 695 (1987); V. Müller, H.-J. Schmidt, and A.A. Starobinsky. *Phys. Lett. B* **1987**, *202*, 198.
56. Chiba, T.; Smith, T.L.; Erickcek, A.L. Solar System constraints to general $f(R)$ gravity. *Phys. Rev. D* **2007**, *75*, 124014. [[CrossRef](#)]
57. Hu, W.; Sawicki, I. Models of $f(R)$ cosmic acceleration that evade solar system tests. *Phys. Rev. D* **2007**, *76*, 064004. [[CrossRef](#)]
58. Starobinsky, A.A. Disappearing cosmological constant in $f(R)$ gravity. *JETP Lett.* **2007**, *86*, 157–163. [[CrossRef](#)]
59. Tsujikawa, S. Observational signatures of $f(R)$ dark energy models that satisfy cosmological and local gravity constraints. *Phys. Rev. D* **2008**, *77*, 023507. [[CrossRef](#)]
60. Cognola, G.; Elizalde, E.; Nojiri, S.; Odintsov, S.D.; Sebastiani, L.; Zerbini, S. Class of viable modified $f(R)$ gravities describing inflation and the onset of accelerated expansion. *Phys. Rev. D* **2008**, *77*, 046009. [[CrossRef](#)]
61. Abdelwahab, M.; Carloni, S.; Dunsby, P.K.S. Cosmological dynamics of 'exponential gravity'. *Class. Quantum Gravity* **2008**, *25*, 135002. [[CrossRef](#)]
62. Bamba, K.; Geng, C.Q.; Lee, C.C. Cosmological evolution in exponential gravity. *J. Cosmol. Astropart. Phys.* **2010**, *2010*, 021. [[CrossRef](#)]
63. Astashenok, A.V.; Capozziello, S.; Odintsov, S.D.; Oikonomou, V. Causal limit of neutron star maximum mass in $f(R)$ gravity in view of GW190814. *Phys. Lett. B* **2021**, *816*, 136222. [[CrossRef](#)]
64. Rincón, Á.; Panotopoulos, G.; Lopes, I. Anisotropic stars made of exotic matter within the complexity factor formalism. *Eur. Phys. J. C* **2023**, *83*, 116. [[CrossRef](#)]
65. Panotopoulos, G.; Rincón, Á.; Lopes, I. Interior solutions of relativistic stars with anisotropic matter in scale-dependent gravity. *Eur. Phys. J. C* **2021**, *81*, 63. [[CrossRef](#)]
66. Tangphati, T.; Pradhan, A.; Banerjee, A.; Panotopoulos, G. Anisotropic stars in 4D Einstein–Gauss–Bonnet gravity. *Phys. Dark Universe* **2021**, *33*, 100877. [[CrossRef](#)]
67. Andrade, J.; Contreras, E. Stellar models with like-Tolman IV complexity factor. *Eur. Phys. J. C* **2021**, *81*, 889. [[CrossRef](#)]
68. Maurya, S.K.; Tello-Ortiz, F. Anisotropic fluid spheres in the framework of $f(R, T)$ gravity theory. *Ann. Phys.* **2020**, *414*, 168070. [[CrossRef](#)]

Disclaimer/Publisher's Note: The statements, opinions and data contained in all publications are solely those of the individual author(s) and contributor(s) and not of MDPI and/or the editor(s). MDPI and/or the editor(s) disclaim responsibility for any injury to people or property resulting from any ideas, methods, instructions or products referred to in the content.